© ESO 2014

Planck 2013 results. XXI. All-sky Compton parameter power spectrum and high-order statistics

Planck Collaboration: P. A. R. Ade[89], N. Aghanim[63], C. Armitage-Caplan[95], M. Arnaud[76], M. Ashdown[73,6], F. Atrio-Barandela[20], J. Aumont[63], C. Baccigalupi[88], A. J. Banday[98,10], R. B. Barreiro[70], J. G. Bartlett[1,71], E. Battaner[100], K. Benabed[64,97], A. Benoît[61], A. Benoit-Lévy[27,64,97], J.-P. Bernard[98,10], M. Bersanelli[37,54], P. Bielewicz[98,10,88], J. Bobin[76], J. J. Bock[71,11], A. Bonaldi[72], J. R. Bond[9], J. Borrill[15,92], F. R. Bouchet[64,97], M. Bridges[73,6,67], M. Bucher[1], C. Burigana[53,35], R. C. Butler[53], J.-F. Cardoso[77,1,64], P. Carvalho[6], A. Catalano[78,75], A. Challinor[67,73,12], A. Chamballu[76,17,63], H. C. Chiang[30,7], L.-Y Chiang[66], P. R. Christensen[84,40], S. Church[94], D. L. Clements[59], S. Colombi[64,97], L. P. L. Colombo[26,71], B. Comis[78], F. Couchot[74], A. Coulais[75], B. P. Crill[71,85], A. Curto[6,70], F. Cuttaia[53], A. Da Silva[13], L. Danese[88], R. D. Davies[72], R. J. Davis[72], P. de Bernardis[36], A. de Rosa[53], G. de Zotti[49,88], J. Delabrouille[1], J.-M. Delouis[64,97], F.-X. Désert[57], C. Dickinson[72], J. M. Diego[70], K. Dolag[99,81], H. Dole[63,62], S. Donzelli[54], O. Doré[71,11], M. Douspis[63], X. Dupac[43], G. Efstathiou[67], T. A. Enßlin[81], H. K. Eriksen[68], F. Finelli[53,55], I. Flores-Cacho[10,98], O. Forni[98,10], M. Frailis[51], E. Franceschi[53], S. Galeotta[51], K. Ganga[1], R. T. Génova-Santos[69], M. Giard[98,10], G. Giardino[44], Y. Giraud-Héraud[1], J. González-Nuevo[70,88], K. M. Górski[71,101], S. Gratton[73,67], A. Gregorio[38,51], A. Gruppuso[53], F. K. Hansen[68], D. Hanson[82,71,9], D. Harrison[67,73], S. Henrot-Versillé[74], C. Hernández-Monteagudo[14,81], D. Herranz[70], S. R. Hildebrandt[11], E. Hivon[64,97], M. Hobson[6], W. A. Holmes[71], A. Hornstrup[18], W. Hovest[81], K. M. Huffenberger[28], G. Hurier[63,78], A. H. Jaffe[59], T. R. Jaffe[98,10], W. C. Jones[30], M. Juvela[29], E. Keihänen[29], R. Keskitalo[24,15], T. S. Kisner[80], R. Kneissl[42,8], J. Knoche[81], L. Knox[31], M. Kunz[19,63,3], H. Kurki-Suonio[29,47], F. Lacasa[63], G. Lagache[63], A. Lähteenmäki[2,47], J.-M. Lamarre[75], A. Lasenby[6,73], R. J. Laureijs[44], C. R. Lawrence[71], J. P. Leahy[72], R. Leonardi[43], J. León-Tavares[45,2], J. Lesgourgues[96,87], M. Liguori[34], P. B. Lilje[68], M. Linden-Vørnle[18], M. López-Caniego[70], P. M. Lubin[32], J. F. Macías-Pérez[78], B. Maffei[72], D. Maino[37,54], N. Mandolesi[53,5,35], A. Marcos-Caballero[70], M. Maris[51], D. J. Marshall[76], P. G. Martin[9], E. Martínez-González[70], S. Masi[36], M. Massardi[52], S. Matarrese[34], F. Matthai[81], P. Mazzotta[39], A. Melchiorri[36,56], J.-B. Melin[17], L. Mendes[43], A. Mennella[37,54], M. Migliaccio[67,73], S. Mitra[58,71], M.-A. Miville-Deschênes[63,9], A. Moneti[64], L. Montier[98,10], G. Morgante[53], D. Mortlock[59], A. Moss[90], D. Munshi[89], P. Naselsky[84,40], F. Nati[36], P. Natoli[35,4,53], C. B. Netterfield[22], H. U. Nørgaard-Nielsen[18], F. Noviello[72], D. Novikov[59], I. Novikov[84], S. Osborne[94], C. A. Oxborrow[18], F. Paci[88], L. Pagano[36,56], F. Pajot[63], D. Paoletti[53,55], B. Partridge[46], F. Pasian[51], G. Patanchon[1], O. Perdereau[74], L. Perotto[78], F. Perrotta[88], F. Piacentini[36], M. Piat[1], E. Pierpaoli[26], D. Pietrobon[71], S. Plaszczynski[74], E. Pointecouteau[98,10], G. Polenta[4,50], N. Ponthieu[63,57], L. Popa[65], T. Poutanen[47,29,2], G. W. Pratt[76], G. Prézeau[11,71], S. Prunet[64,97], J.-L. Puget[63], J. P. Rachen[23,81], R. Rebolo[69,16,41], M. Reinecke[81], M. Remazeilles[72,63,1], C. Renault[78], S. Ricciardi[53], T. Riller[81], I. Ristorcelli[98,10], G. Rocha[71,11], C. Rosset[1], M. Rossetti[37,54], G. Roudier[1,75,71], J. A. Rubiño-Martín[69,41], B. Rusholme[60], M. Sandri[53], D. Santos[78], G. Savini[86], D. Scott[25], M. D. Seiffert[71,11], E. P. S. Shellard[12], L. D. Spencer[89], J.-L. Starck[76], V. Stolyarov[6,73,93], R. Stompor[1], R. Sudiwala[89], R. Sunyaev[81,91], F. Sureau[76], D. Sutton[67,73], A.-S. Suur-Uski[29,47], J.-F. Sygnet[64], J. A. Tauber[44], D. Tavagnacco[51,38], L. Terenzi[53], L. Toffolatti[21,70], M. Tomasi[54], M. Tristram[74], M. Tucci[19,74], J. Tuovinen[83], G. Umana[48], L. Valenziano[53], J. Valiviita[47,29,68], B. Van Tent[79], J. Varis[83], P. Vielva[70], F. Villa[53], N. Vittorio[39], L. A. Wade[71], B. D. Wandelt[64,97,33], S. D. M. White[81], D. Yvon[17], A. Zacchei[51], and A. Zonca[32]

(Affiliations can be found after the references)

Preprint online version: December 1, 2014

ABSTRACT

We have constructed the first all-sky map of the thermal Sunyaev-Zeldovich (tSZ) effect by applying specifically tailored component separation algorithms to the 100 to 857 GHz frequency channel maps from the *Planck* survey. This map shows an obvious galaxy cluster tSZ signal that is well matched with blindly detected clusters in the *Planck* SZ catalogue. To characterize the signal in the tSZ map we have computed its angular power spectrum. At large angular scales ($\ell < 60$), the major foreground contaminant is the diffuse thermal dust emission. At small angular scales ($\ell > 500$) the clustered cosmic infrared background (CIB) and residual point sources are the major contaminants. These foregrounds are carefully modelled and subtracted. We thus measure the tSZ power spectrum over angular scales $0.17° \lesssim \theta \lesssim 3.0°$ that were previously unexplored. The measured tSZ power spectrum is consistent with that expected from the *Planck* catalogue of SZ sources, with clear evidence of additional signal from unresolved clusters and, potentially, diffuse warm baryons. Marginalized band-powers of the *Planck* tSZ power spectrum and the best-fit model are given. We use the tSZ power spectrum to obtain the following cosmological constraint: $\sigma_8(\Omega_m/0.28)^{0.40} = 0.784 \pm 0.016\,(68\,\%\,\text{C.L.})$. This result is in weak tension (at $2.7\,\sigma$) with the *Planck* measurements of the primary anisotropies in the cosmic microwave background. The non-Gaussianity of the Compton parameter map is further characterized by computing its 1D probability distribution function and its bispectrum. These are used to place additional independent constraints on σ_8.

Key words. cosmological parameters – large-scale structure of Universe – Galaxies: clusters: general

1. Introduction

This paper, one of a set associated with the 2013 release of data from the *Planck*[1] mission (Planck Collaboration I 2013), describes the construction of a Compton *y* parameter map and the determination of its angular power spectrum and high-order statistics.

The thermal Sunyaev-Zeldovich (tSZ) effect (Sunyaev & Zeldovich 1972), produced by the inverse Compton scattering of cosmic microwave background (CMB) photons by hot electrons along the line of sight, has proved to be a major tool for studying the physics of clusters of galaxies as well as structure formation in the Universe. In particular, tSZ-selected catalogues of clusters of galaxies have been provided by various experiments including the *Planck* satellite (Planck Collaboration VIII 2011; Planck Collaboration XXIX 2013), the Atacama Cosmology Telescope (ACT, Hasselfield et al. 2013) and the South Pole Telescope (SPT, Reichardt et al. 2013). These catalogues and their associated sky surveys have been used to study the physics of clusters of galaxies (Planck Collaboration XII 2011; Planck Collaboration XI 2011; Planck Collaboration X 2011) and their cosmological implications (Planck Collaboration XX 2013; Benson et al. 2013; Das et al. 2013; Wilson et al. 2012; Mak & Pierpaoli 2012).

The study of number counts and their evolution with redshift using tSZ detected clusters of galaxies is an important cosmological test (Carlstrom et al. 2002; Dunkley et al. 2013; Benson et al. 2013; Planck Collaboration XX 2013). The measurement of the tSZ effect power spectrum has been proposed by Komatsu & Seljak (2002) as a complement to the counts. One advantage of using the tSZ angular power spectrum over cluster counts is that no explicit measurement of cluster masses is required. Also, lower mass, and therefore fainter, clusters, which may not be detected as individual objects, contribute to this statistical signal (Battaglia et al. 2010; Shaw et al. 2010). However, significant drawbacks of using the tSZ angular power spectrum include potential contamination from point sources (Rubiño-Martín & Sunyaev 2003; Taburet et al. 2010) and other foregrounds.

To date, measurements of the tSZ power spectrum are only available from high resolution CMB-oriented experiments like ACT (Sievers et al. 2013) and SPT (Reichardt et al. 2012). In these studies, constraints on the amplitude of the tSZ power spectrum at $\ell = 3000$ are obtained by fitting a tSZ template in addition to other components (i.e., CMB, radio and infrared point-source and clustered cosmic infrared background, CIB) to the measured total power spectrum. These constraints are obtained at angular scales where the tSZ signal dominates over the CMB, but at these same scales the contamination from point sources and the clustered CIB is important and may affect the measured tSZ signal. Moreover, the scales probed are particularly sensitive to the uncertainties in modelling the intracluster medium (ICM) over a broad range of masses and redshifts, and at large cluster-centric radii (Battaglia et al. 2010). Recent work, using hydrodynamical simulations (Battaglia et al. 2010; Battaglia et al. 2012) *N*-body simulations plus semi-analytic gas models (Trac et al. 2011) and purely analytic models (Shaw et al. 2010), have significantly reduced the tension between the observed and predicted values. However the distribution of amplitudes between differ-

---

Table 1. Conversion factors for tSZ Compton parameter *y* to CMB temperature units and the FWHM of the beam of the *Planck* channel maps.

Frequency [GHz]	$T_{\rm CMB} \, g(\nu)$ [$K_{\rm CMB}$]	FWHM [arcmin]
100	−4.031	9.66
143	−2.785	7.27
217	0.187	5.01
353	6.205	4.86
545	14.455	4.84
857	26.335	4.63

ent models and simulations is still significantly larger than the measurement errors, degrading the constraints that can be placed on cosmological parameters with these methods (Dunkley et al. 2013; Reichardt et al. 2013).

In addition to the power spectrum, and (as pointed out in Rubiño-Martín & Sunyaev 2003), the skewness or, equivalently, the bispectrum of the tSZ signal is a powerful and independent tool to study and to isolate the signal of clusters, separating it from the contribution of radio and IR sources. Recently, Bhattacharya et al. (2012) showed that the bispectrum of the tSZ effect signal is dominated by massive clusters at intermediate redshifts, for which high-precision X-ray observations exist. This contrasts with the power spectrum, where the signal mainly comes from the lower mass and higher redshift groups and clusters (e.g., Trac et al. 2011). The theoretical uncertainty in the tSZ bispectrum is thus expected to be significantly smaller than that of the SZ power spectrum. Combined measurements of the power spectrum and the bispectrum can thus be used to distinguish the contribution to the power spectrum from different cluster masses and redshift ranges. The bispectrum amplitude scales as σ_8^{10-12} (Bhattacharya et al. 2012). Measurements of the tSZ bispectrum have been reported by the SPT collaboration (Crawford et al. 2013). Alternatively, Wilson et al. (2012) used the unnormalized skewness of the tSZ fluctuations, $\langle T^3(\mathbf{n}) \rangle$, which scales approximately as σ_8^{11}, to obtain an independent determination of σ_8.

Thanks to its all-sky coverage and unprecedented wide frequency range, *Planck* has the unique ability to produce an all-sky tSZ Compton parameter (*y*) map and an accurate measurement of the tSZ power spectrum at intermediate and large angular scales, for which the tSZ fluctuations are almost insensitive to the cluster core physics. The *Planck* Compton parameter map also offers the possibility of studying the properties of the non-Gaussianity of the tSZ signal using higher order statistical estimators, such as the skewness and the bispectrum. In this paper we construct a tSZ all-sky map from the individual *Planck* frequency maps and compute its power spectrum, its 1D probability density function (1D PDF), and the associated bispectrum.

The paper is structured as follows. Section 2 describes the *Planck* data used to compute the tSZ all-sky map and the simulations used to characterize it. We discuss details of the modelling of the tSZ effect power spectrum and bispectrum in Sect. 3. In Sect. 4 we present the *Planck* all-sky Compton parameter map. Section 5 describes the power spectrum analysis. Cross-checks using high-order statistics are presented in Sect. 6. Cosmological interpretation of the results is discussed in Sect. 7, and we present our conclusions in Sect. 8.

2. Data and simulations

2.1. The Planck data

This paper is based on the first 15.5 months of *Planck*'s mission, corresponding to more than two full-sky surveys. We refer to Planck Collaboration II (2013), Planck Collaboration III (2013), Planck Collaboration V (2013), Planck Collaboration VIII (2013), Planck Collaboration IX (2013), and Planck Collaboration VI (2013) for the generic scheme of time-ordered information processing and map-making, as well as for the technical characteristics of the *Planck* frequency maps. The *Planck* channel maps are provided in HEALPix (Górski et al. 2005) pixelization scheme at $N_{\rm side} = 2048$. An error map is associated with each channel map and is obtained from the difference of maps made from the first and second half of each ring (stable pointing period). The difference maps, called half-ring or null maps, are mainly free from astrophysical emission and they are a good representation of the statistical instrumental noise. Null maps have also been used to estimate the noise in the final Compton parameter maps. Here we approximate the *Planck* effective beams by circular Gaussians (Planck Collaboration IV 2013; Planck Collaboration VII 2013) The FWHM values for each frequency channel are given in Table 1. Although tests have been performed using both LFI and HFI channel maps, the work presented here is based mostly on HFI data.

2.2. FFP6 Simulations

We also use simulated *Planck* frequency maps obtained from the Full Focal Plane (FFP6) simulations, which are described in the *Planck* Explanatory Supplement (Planck Collaboration ES 2013). These simulations include the most relevant sky components at microwave and millimetre frequencies, based on foregrounds from the *Planck* Sky Model (PSM, Delabrouille et al. 2013): CMB; thermal SZ effect; diffuse Galactic emissions (synchrotron, free-free, thermal and spinning dust and CO); radio and infrared point sources, and the clustered CIB. The simulated tSZ signal was constructed using hydrodynamical simulations of clusters of galaxies up to redshift 0.3, completed with pressure profile-based simulations of individual clusters of galaxies randomly drawn on the sky. The noise in the maps was obtained from realizations of Gaussian random noise in the time domain and therefore accounts for noise inhomogeneities in the maps.

3. Modelling the tSZ effect

The thermal SZ Compton parameter in a given direction, $\boldsymbol{n}$, is

$$y(\boldsymbol{n}) = \int n_{\rm e} \frac{k_{\rm B} T_{\rm e}}{m_{\rm e} c^2} \sigma_{\rm T}\, {\rm d}s, \tag{1}$$

where $k_{\rm B}$ is the Boltzmann contant, $m_{\rm e}$ the electron mass, $\sigma_{\rm T}$ the Thomson cross-section, ${\rm d}s$ the distance along the line of sight, $\boldsymbol{n}$, and $n_{\rm e}$ and $T_{\rm e}$ are the electron number density and temperature.

In units of CMB temperature the contribution of the tSZ effect to the *Planck* maps for a given frequency ν is

$$\frac{\Delta T}{T_{\rm CMB}} = g(\nu)\, y. \tag{2}$$

Neglecting relativistic corrections we have $g(\nu) = [x \coth(x/2) - 4]$, with $x = h\nu/(k_{\rm B} T_{\rm CMB})$. Table 1 shows the conversion factors for Compton parameter to CMB temperature, $K_{\rm CMB}$, for each frequency channel after integrating over the bandpass.

3.1. tSZ power spectrum

Decomposing the map in spherical harmonics, $Y_{\ell m}$, we obtain

$$y(\boldsymbol{n}) = \sum_{\ell m} y_{\ell m}\, Y_{\ell m}(\boldsymbol{n}). \tag{3}$$

Thus, the angular power spectrum of the Compton parameter map is

$$C_\ell^{\rm tSZ} = \frac{1}{2\,\ell + 1} \sum_m y_{\ell m} y_{\ell m}^*. \tag{4}$$

Note that $C_\ell^{\rm tSZ}$ is a dimensionless quantity here, like y.

To model the tSZ power spectrum we consider a 2-halo model to account for intra-halo and inter-halo correlations:

$$C_\ell^{\rm SZ} = C_\ell^{\rm 1halo} + C_\ell^{\rm 2halos}. \tag{5}$$

The 1-halo term, also known as the Poissonian contribution, can be computed by summing the square of the Fourier transform of the projected SZ profile, weighted by the number density of clusters of a given mass and redshift (Komatsu & Seljak 2002):

$$C_\ell^{\rm 1halo} = \int_0^{z_{\rm max}} dz\, \frac{dV_{\rm c}}{dz d\Omega} \int_{M_{\rm min}}^{M_{\rm max}} dM\, \frac{dn(M,z)}{dM}\, |\tilde{y}_\ell(M,z)|^2, \tag{6}$$

where $dV_{\rm c}/(dz d\Omega)$ is the comoving volume per unit redshift and solid angle and $n(M,z)dM\, dV_{\rm c}/(dz d\Omega)$ is the probability of having a galaxy cluster of mass M at a redshift z in the direction $d\Omega$. The quantity $\tilde{y}_\ell = \tilde{y}_\ell(M,z)$ is the 2D Fourier transform on the sphere of the 3D radial profile of the Compton y-parameter of individual clusters,

$$\tilde{y}_\ell(M,z) = \frac{4\pi r_{\rm s}}{l_{\rm s}^2} \left(\frac{\sigma_{\rm T}}{m_{\rm e} c^2}\right) \int_0^\infty dx\, x^2 P_{\rm e}(M,z,x) \frac{\sin(\ell x/\ell_{\rm s})}{\ell_x/\ell_{\rm s}} \tag{7}$$

where $x = r/r_{\rm s}$, $\ell_{\rm s} = D_{\rm A}(z)/r_{\rm s}$, $r_{\rm s}$ is the scale radius of the 3D pressure profile, $D_{\rm A}(z)$ is the angular diameter distance to redshift z and $P_{\rm e}$ is the electron pressure profile.

The 2-halo term is obtained by computing the correlation between two different halos (Komatsu & Kitayama 1999; Diego & Majumdar 2004; Taburet et al. 2011):

$$C_\ell^{\rm 2halos} = \int_0^{z_{\rm max}} dz\, \frac{dV_{\rm c}}{dz d\Omega} \times$$
$$\left[\int_{M_{\rm min}}^{M_{\rm max}} dM\, \frac{dn(M,z)}{dM}\, |\tilde{y}_\ell(M,z)|\, B(M,z)\right]^2 P(k,z), \tag{8}$$

where $P(k,z)$ is the 3D matter power spectrum at redshift z. Here $B(M,z)$ is the time-dependent linear bias factor that relates the matter power spectrum, $P(k,z)$, to the power spectrum of the cluster correlation function. Following Komatsu & Kitayama (1999, see also Mo & White 1996) we adopt $B(M,z) = 1 + (\nu^2(M,z) - 1)/\delta_{\rm c}(z)$, where $\nu(M,z) = \delta_{\rm c}(M)/D(z)\sigma(M)$, $\sigma(M)$ is the present-day rms mass fluctuation, $D(z)$ is the linear growth factor, and $\delta_{\rm c}(z)$ is the threshold over-density of spherical collapse.

Finally, we compute the tSZ power spectrum using the Tinker et al. (2008) mass function $dn(M,z)/dM$ including an observed-to-true mass bias of 20%, as discussed in detail in Planck Collaboration XX (2013), and we model the SZ Compton parameter using the pressure profile of Arnaud et al. (2010). This approach is adopted in order to be consistent with the ingredients of the cluster number count analysis in Planck Collaboration XX (2013).

3.2. *N*th *moment of the tSZ field*

To calculate the *N*th moment of the tSZ field, we assume, to first order, that the distribution of clusters on the sky can be adequately described by a Poisson distribution corresponding to the 1-halo term. We neglect the contribution due to clustering between clusters and their overlap (Komatsu & Kitayama 1999). The *N*th moment is then given by (Wilson et al. 2012)

$$\int_0^{z_{max}} dz \frac{dV_c}{dz d\Omega} \int_{M_{min}}^{M_{max}} dM \frac{dn(M,z)}{dM} \int d^2\theta \, y(\theta,M,z)^N, \tag{9}$$

where $y(\theta, M, z)$ is the integrated Compton parameter along the line of sight for a cluster of mass M at redshift z.

3.3. Bispectrum

The angular bispectrum, analogous to the 3-point correlation function in harmonic space, is the lowest-order indicator of the non-Gaussianity of a field. It is given by

$$B_{\ell_1 \ell_2 \ell_3}^{m_1 m_2 m_3} = \langle y_{\ell_1 m_1} y_{\ell_2 m_2} y_{\ell_3 m_3} \rangle, \tag{10}$$

where the angle-averaged quantity in the full-sky limit can be written as

$$b(\ell_1, \ell_2, \ell_3) = \sum_{m_1 m_2 m_3} \begin{pmatrix} \ell_1 & \ell_2 & \ell_3 \\ m_1 & m_2 & m_3 \end{pmatrix} B_{\ell_1 \ell_2 \ell_3}^{m_1 m_2 m_3}, \tag{11}$$

which has to satisfy the conditions $m_1 + m_2 + m_3 = 0$, $\ell_1 + \ell_2 + \ell_3 =$ even, and $\left| \ell_i - \ell_j \right| \le \ell_k \le \ell_i + \ell_j$, for the Wigner $3j$ function in brackets. For illustration we compute the bispectrum assuming a Poissonian distribution, given by (Bhattacharya et al. 2012)

$$b(\ell_1, \ell_2, \ell_3) \approx \sqrt{\frac{(2\ell_1 + 1)(2\ell_2 + 1)(2\ell_3 + 1)}{4\pi}} \begin{pmatrix} \ell_1 & \ell_2 & \ell_3 \\ 0 & 0 & 0 \end{pmatrix}$$
$$\int_0^{z_{max}} dz \frac{dV_c}{dz d\Omega} \int_{M_{min}}^{M_{max}} dM \frac{dn(M,z)}{dM} \tilde{y}_{\ell_1}(M,z) \tilde{y}_{\ell_2}(M,z) \tilde{y}_{\ell_3}(M,z). \tag{12}$$

4. The reconstructed all-sky tSZ map

4.1. Reconstruction methods

The contribution of the tSZ effect in the *Planck* frequency maps is subdominant with respect to the CMB and other foreground emissions. Furthermore, the tSZ effect from galaxy clusters is spatially localized and leads to a highly non-Gaussian signal with respect to that from the CMB. CMB-oriented component-separation methods (Planck Collaboration XII 2013) are not optimized to recover the tSZ signal. We therefore need to use specifically tailored component separation algorithms that are able to reconstruct the tSZ signal from the *Planck* frequency channel maps. These optimized all-sky component separation techniques rely on the spatial localization of the different astrophysical components and on their spectral diversity to separate them. We present in the following, the results of two algorithms, MILCA (Modified Internal Linear Combination Algorithm, Hurier et al. 2013) and NILC (Needlet Iindependent Linear Combination, Remazeilles et al. 2011). Both are based on the well known Internal Linear Combination (ILC) approach that searches for the linear combination of the input maps that minimizes the variance of the final reconstructed map under the constraint of offering unit gain to the component of interest (here the tSZ effect, whose frequency dependence is known). Both algorithms have been extensively tested on simulated *Planck* data.

4.1.1. MILCA

MILCA (Hurier et al. 2013) uses two constraints: preservation of the tSZ signal, assuming the tSZ spectral signature; and removal of the CMB contamination in the final SZ map, making use of the well known spectrum of the CMB. In addition, to compute the weights of the linear combination, we have used the extra degrees of freedom in the linear system to minimize residuals from other components (two degrees of freedom) and from the noise (two additional degrees). The noise covariance matrix was estimated from the null maps described in Section 2.1. To improve the efficiency of the MILCA algorithm, weights are allowed to vary as a function of multipole ℓ, and are computed independently on different sky regions. We have used 11 filters in ℓ space, with an overall transmission of one, except for $\ell < 8$. For these large angular scales we have used a Gaussian filter to reduce foreground contamination. The size of the independent sky regions was adapted to the multipole range to ensure sufficient spatial localization at the required resolution. We used a minimum of 12 regions at low resolution and a maximum of 3072 regions at high resolution.

4.1.2. NILC

In the multi-component extensions of NILC (Delabrouille et al. 2009; Remazeilles et al. 2011), initially developed to extract the CMB, the weights for component separation (i.e., covariances) are computed independently in domains of a needlet decomposition (in the spherical wavelet frame). The needlet decomposition provides localization of the ILC filters both in pixel and in multipole space, allowing us to deal with local contamination conditions varying both in position and in scale. We imposed constraints to remove the CMB contamination and preserve the tSZ effect. To avoid strong foreground effects, the Galactic plane was masked before applying NILC to the *Planck* frequency maps.

In both methods, we mask the brightest regions in the *Planck* 857 GHz channel map, corresponding to about 33% of the sky. We use the HFI channel maps from 100 to 857 GHz that are convolved to a common resolution of 10′. The 857 GHz map is mainly exploited in the internal linear combination as a template to remove the thermal dust emission on large angular scales. However, this induces significant CIB residuals in the tSZ map on small scales. To avoid this contamination, while enabling efficient removal of the diffuse thermal dust emission at large angular scales, we use the 857 GHz channel only for $\ell < 300$.
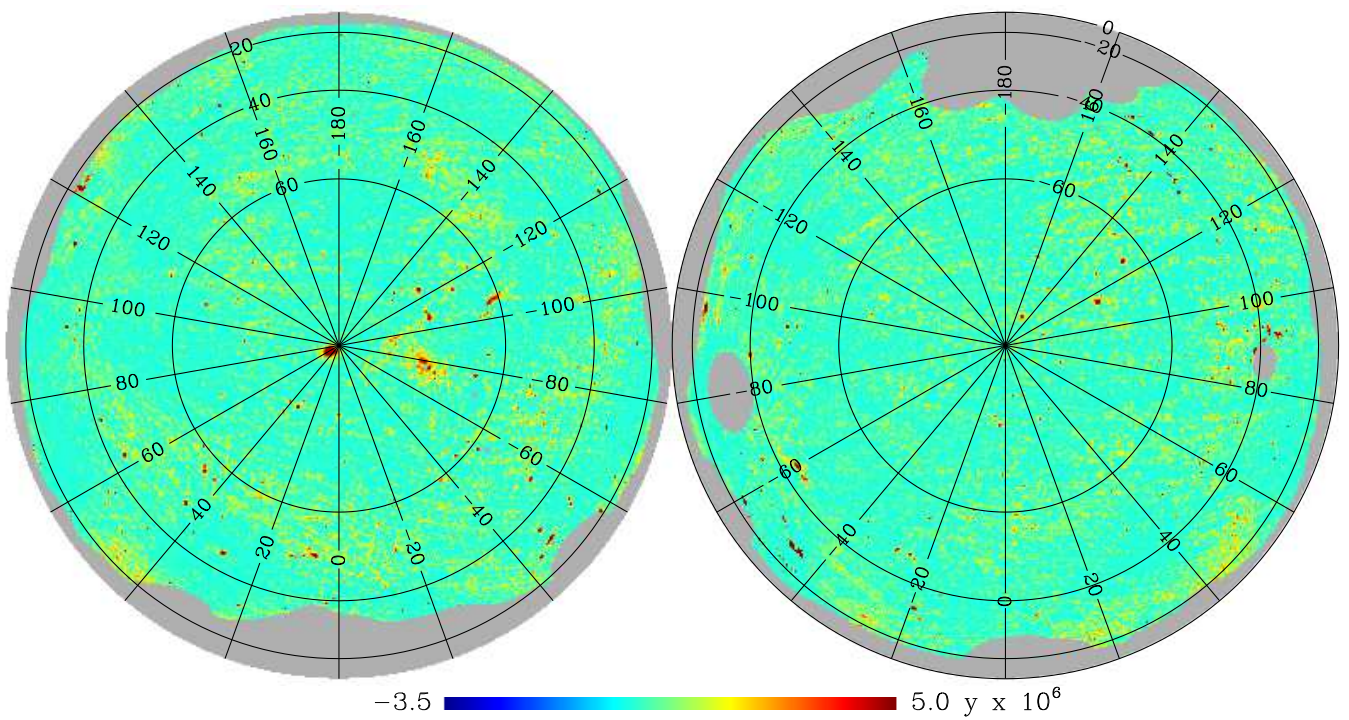
4.2. Reconstructed Compton parameter *y* map

Figure 1 shows the reconstructed *Planck* all-sky Compton parameter map for NILC (top panel) and MILCA (bottom panel). For display purposes, the maps are filtered using the procedure described in Sect. 6. Clusters appear as positive sources: the Coma cluster and Virgo supercluster are clearly visible near the north Galactic pole. As mentioned above, the Galactic plane is masked in both maps, leaving 67% of the sky. Other weaker and more compact clusters are visible in the zoomed region of the Southern cap, shown in the bottom panel of Fig. 2. Strong Galactic and extragalactic radio sources show up as negative bright spots on the maps and were masked prior to any scientific analysis, as discussed below in Sect. 4.3. Residual Galactic contamination is also visible around the edges of the masked area; extra masking was performed to avoid this highly contaminated area. The apparent difference of contrast observed between the NILC and MILCA maps comes from differences in the instru-

NILC tSZ map

-3.5 5.0 y x 10^6

MILCA tSZ map

-3.5 5.0 y x 10^6
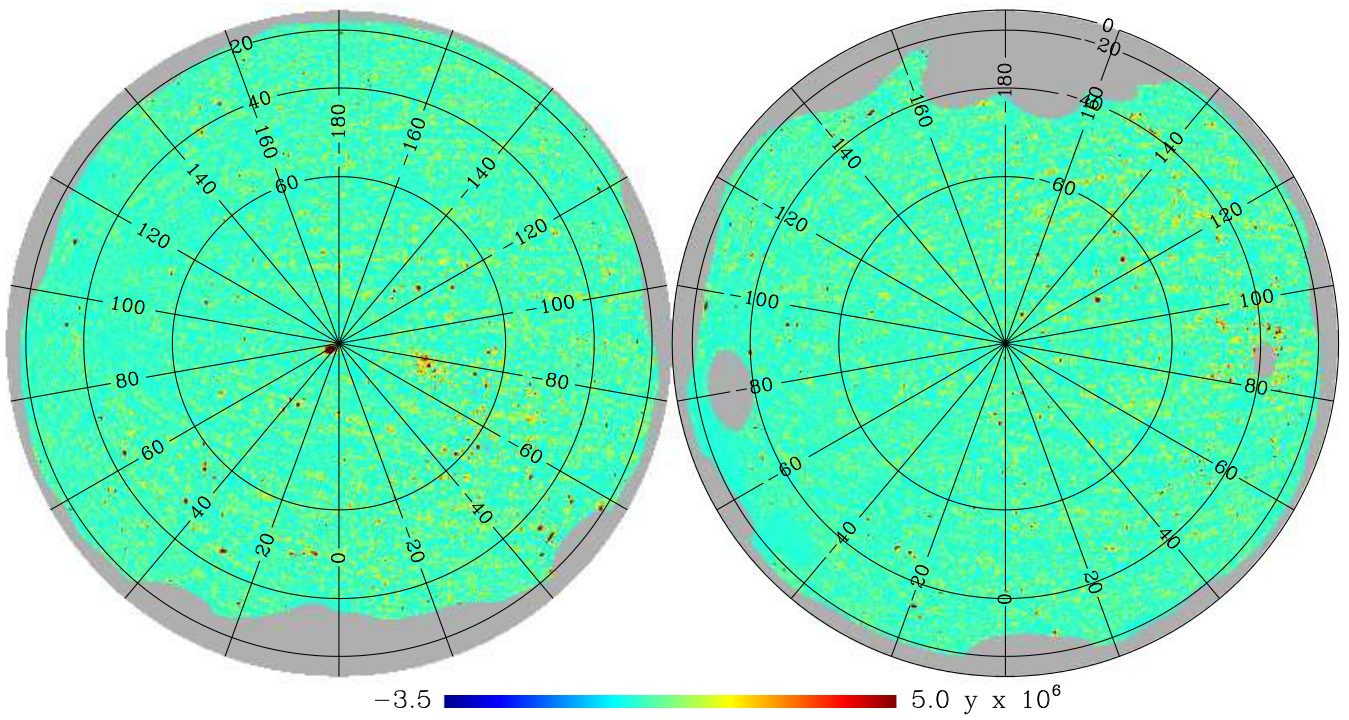
Fig. 1. Reconstructed *Planck* all-sky Compton parameter maps for NILC (*top*) and MILCA (*bottom*) in orthographic projections. The apparent difference in contrast observed between 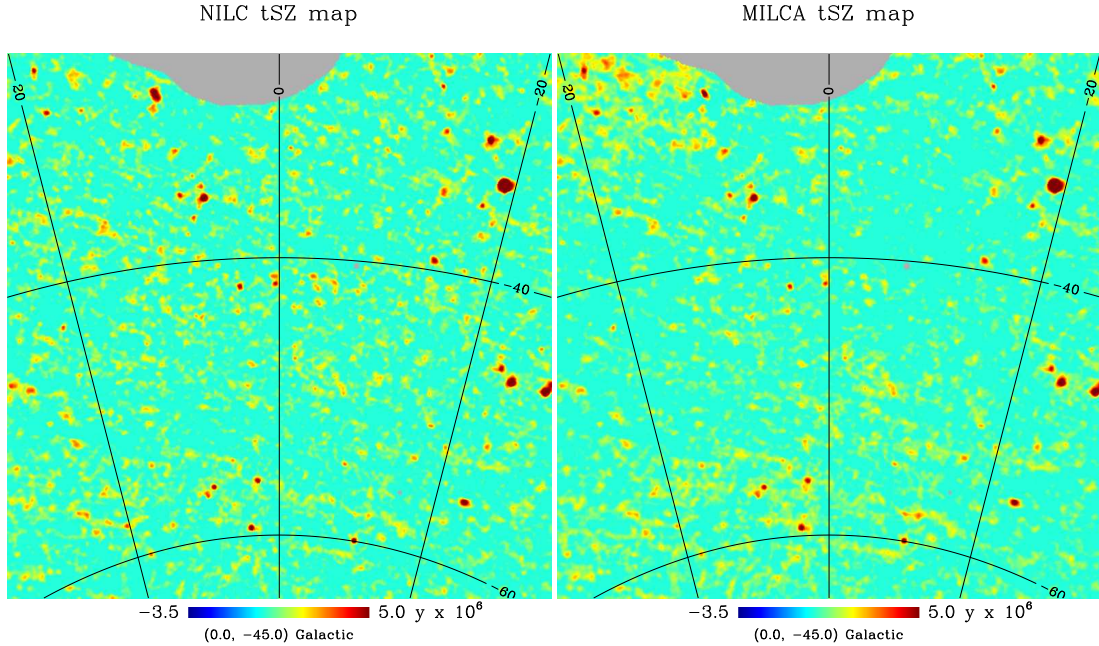the NILC and MILCA maps comes from differences in the instrumental noise contribution and foreground contamination and from the differences in the filtering applied for display purpose to the original Compton parameter maps.

NILC tSZ map   MILCA tSZ map

Fig. 2. A small region of the reconstructed *Planck* all-sky Compton parameter maps for `NILC` (left) and `MILCA` (right) at intermediate Galactic latitudes in the southern sky.

mental noise and foreground contamination (the `NILC` map is slightly noisier but less affected by residual foreground emission than the `MILCA` map, as discussed in Sect. 5.2) and from the differences in the filtering applied for display purposes to the original Compton parameter maps, as discussed in Sect. 6.1.

In addition to the full Compton parameter maps, we also produce the so-called "FIRST" and "LAST" Compton parameter maps from the first and second halves of the survey rings (i.e., pointing periods). These maps are used for the power spectrum analysis in Sect. 5.

4.3. Point source contamination and masking

Point source contamination is an important issue for the cosmological interpretation of the *Planck* Compton parameter map. Radio sources will show up in the reconstructed tSZ maps as negative peaks, while infrared sources will show up as positive peaks, mimicking the cluster signal. To avoid contamination from these sources we introduce a point source mask (PSMASK, hereafter). This mask is the union of the individual frequency point-source masks discussed in Planck Collaboration XXVIII (2013). To test the reliability of this mask we have performed a search for negative sources in the Compton parameter maps using the `MHW2` algorithm (López-Caniego et al. 2006). We found that all detected radio sources in the Compton parameter maps are masked by the PSMASK. For infrared sources, estimating the efficiency of the masking is hampered by the tSZ signal itself. The residual contamination from point sources is discussed in Sects. 5.2 and 6. It is also important to note that the PSMASK may also exclude some clusters of galaxies. This is particularly true in the case of clusters with strong central radio sources, such as the Perseus cluster (see Planck Collaboration XXIX 2013).

4.4. tSZ signal from resolved sources

As a first validation step of the Compton parameter maps we perform a blind search for the SZ signal coming from resolved sources and compare it to the *Planck* catalogue of SZ sources (Planck Collaboration XXIX 2013). The latter comprises 861 confirmed clusters out of 1227 cluster candidates and 54 `CLASS1` highly reliable candidate clusters.

4.4.1. Yields

Two lists of SZ sources above a signal-to-noise ratio threshold of 4.5 are constructed from both `MILCA` and `NILC` all-sky Compton parameter maps outside a 33% Galactic mask. The point source detections are undertaken using two methods.

- `SMATCH`, in which sources are detected using the `SEXtractor` algorithm (Bertin & Arnouts 1996) over the whole sky divided into 504 patches. A single frequency matched filter (Melin et al. 2006a) is then applied to measure the SZ flux density and signal-to-noise ratio using the Arnaud et al. (2010) pressure profile. Using this method, we detect 843 and 872 sources in `MILCA` and `NILC`, respectively.
- `MHWS`, in which SZ sources are detected in the maps using `IFCAMEX` (`MHW2`, González-Nuevo et al. 2006; López-Caniego et al. 2006). The flux density and signal-to-noise ratio are then estimated using `SEXtractor` on $3.65° \times 3.65°$ patches. We detect 1036 and 1740 sources in `MILCA` and `NILC`, respectively, with this method.

The difference between the yields of the two methods is understandable, as `SMATCH` is by construction dedicated to the search for SZ sources and the precise measurement of their flux (including assumptions on the spatial distribution of the SZ signal), whereas `MHWS` targets all types of compact source (includ-
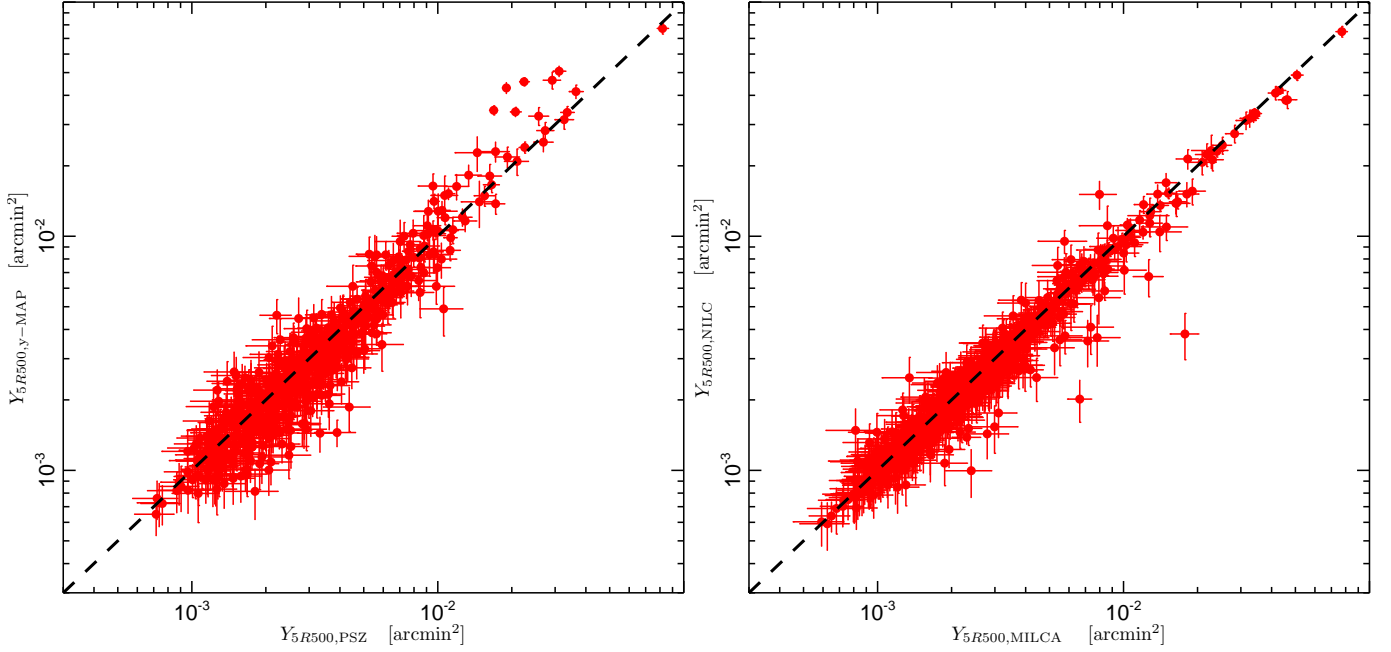
Fig. 3. Comparison of the measurements of Y_{5R500}. *Left*: the values derived from the detection methods used to build the *Planck* catalogue of clusters ($Y_{5R500,PSZ}$), plotted against those from the all-sky reconstructed MILCA tSZ map ($Y_{5R500,y-MAP}$). *Right*: the MILCA ($Y_{5R500,MILCA}$) versus NILC ($Y_{5R500,NILC}$) all-sky tSZ effect maps. The equality relationship is marked as a dashed black line. A least-squares bisector method fit to the data lead to slopes of 1.09 ± 0.02 and 1.08 ± 0.02 for the MILCA and NILC Compton parameter maps, respectively.

ing IR and radio sources) and uses a more "generic" flux estimation procedure.

We have compared these two lists of sources with 790 confirmed clusters and CLASS1 high reliability candidates from the *Planck* catalogue of SZ sources that fall outside the 33% Galactic mask. The association is performed on the basis of the source positions within a search radius of 10′ (the resolution of the SZ all-sky maps). We found 583 and 529 matches in the MILCA source list with the SMATCH and MHWS methods, respectively (614 and 414 from the NILC source list). This match of 52 to 77% per cent, respectively. This is consistent with the results in Melin et al. (2012), which show that indirect detection methods based on reconstructed *y*-maps are less efficient at extracting clusters of galaxies than dedicated direct methods such as those used to build the *Planck* catalogue of SZ sources (i.e., MMF1, MMF3 and PwS, Herranz et al. 2002; Melin et al. 2006b; Carvalho et al. 2012; Planck Collaboration XXIX 2013).

4.4.2. Photometry

Of more importance than a comparison of yields is the comparison in terms of photometry. For all-sky map detections that are associated with clusters in the *Planck* SZ catalogue, the SZ flux measurement from the all-sky maps correlates very well with the maximum likelihood value of the integrated Compton parameter, $Y_{5R500}{}^{2}$, provided by the dedicated SZ-detection methods in the *Planck* SZ catalogue. As shown in the left panel of Fig. 3, the correlation is very tight, with little dispersion (0.1 dex). We note that the few points at high Y_{5R500} that lie significantly above the one-to-one line are not unexpected; they correspond to nearby and extended clusters. On the one hand, the significance of SZ flux measurement increases with the flux. On the other hand, the

---

^{2} R_{500} refers to the radius inside which the mean density is 500 times the critical density at the cluster redshift.

catalogue detection methods are not optimized for the extraction of such extended sources (see Planck Collaboration XXIX 2013, for details). Therefore they tend to miss part of the SZ flux, which is recovered, together with a better estimate of the cluster size, from the Compton parameter map directly.

As a sanity check, we have also matched the list of sources detected by a given method using both MILCA and NILC maps in order to compare the SZ photometry. The right panel of Fig. 3 shows very good agreement between the methods. There is only 0.07 and 0.01 dex dispersion between them for the SMATCH and MHWS extraction methods, respectively.

Together, these results indicate that we can be confident in the fidelity with which the tSZ signal is reconstructed over the whole sky by the MILCA and NILC methods.

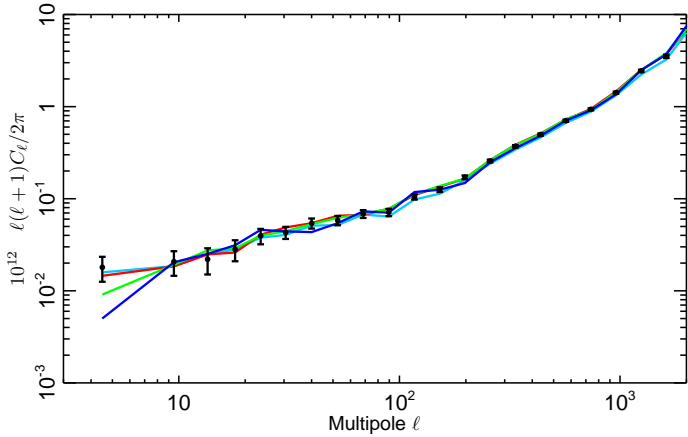## 5. Angular power spectrum of the reconstructed *y*-map

5.1. Methodology

To estimate the power spectrum of the tSZ signal we use the XSPECT method (Tristram et al. 2005) initially developed for the cross-correlation of independent detector maps. XSPECT uses standard MASTER-like techniques (Hivon et al. 2002) to correct for the beam convolution and the pixelization, as well as the mode-coupling induced by masking foreground contaminated sky regions.

We apply XSPECT to the FIRST and LAST *y*-maps obtained using NILC and MILCA. We consider the following map pairs: the MILCA FIRST and LAST (MILCA F/L); the NILC FIRST and LAST (NILC F/L); and the NILC FIRST and MILCA LAST (NILC–MILCA F/L), or equivalently the MILCA FIRST and NILC LAST (MILCA–NILC F/L). As the noise is uncorrelated between the map pairs the resulting power spectrum is not biased and we preserve the variance.
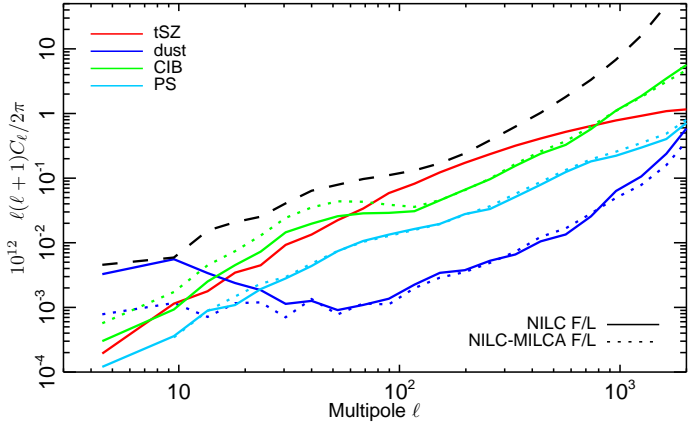
Fig. 4. Angular power spectrum of the main foreground contributions as estimated using the FFP6 simulations. We plot the diffuse Galactic emission (blue), clustered CIB (green) and point source (cyan) contributions, as well as the tSZ signal (red). The solid and dotted lines correspond to the NILC F/L and to the NILC-MILCA F/L cross-power spectra, respectively. For illustration we also show the *Planck* instrumental noise auto-power spectrum (dashed black line) in the MILCA Compton parameter map.

Fig. 5. Angular cross-power spectra of the *Planck* NILC F/L reconstructed Compton parameter maps for different Galactic masks, removing 30% (cyan), 40% (black points and error bars), 50% (red), 60% (green), and 70% (blue) of the sky.

In the following, all the spectra will use a common multipole binning scheme, which was defined in order to minimize the correlation between adjacent bins at low multipoles and to increase the signal-to-noise at high multipole values. Error bars in the spectrum are computed analytically from the auto-power and cross-power spectra of the pairs of maps, as described in Tristram et al. (2005). All of our Compton parameter maps assume a circular Gaussian beam of 10′ FWHM. The additional filtering at large angular scales in the MILCA Compton parameter maps is also accounted for and deconvolved.

5.2. Foreground contamination

The challenge in computing the tSZ power spectrum is to estimate and minimize foreground contamination. We do not intend here to provide a detailed foreground analysis, but rather to identify the main foreground contaminants at different multipoles.

We first identify the dominant foregrounds in the reconstructed Compton parameter maps. To do so, we apply to the FFP6 simulated maps the linear combination weights of NILC and MILCA derived from the real data. In this way we have constructed maps of the expected foreground contamination in the final Compton parameter maps.

Figure 4 shows the angular power spectra for these reconstructed foreground contamination maps. We use the PSMASK and a conservative common Galactic mask that leaves 50% of the sky. The Galactic mask is constructed by removing the 50% brightest regions of the sky in the 857 GHz intensity map, as detailed below in Sect. 5.2.1. We show the diffuse Galactic contamination (blue), the clustered CIB contamination (green), and point source contamination (cyan). We consider here the foreground contamination in the cross-power spectra of the NILC F/L (dotted lines) and NILC-MILCA F/L maps (solid lines). The tSZ power spectrum for the FFP6 simulations is plotted in red. For illustration we also show the *Planck* instrumental noise power spectrum (dashed black line) in the MILCA Compton parameter map. We clearly observe that, as expected, the diffuse Galactic emission (mainly thermal dust), dominates the foreground contribution at low multipoles. For large multipoles the clustered CIB and point source contributions dominate the power spectrum. However, it is important to notice that the tSZ signal dominates the angular power spectrum in the multiple range $100 < \ell < 800$. We also note that foreground contamination differs depending on the reconstruction method, and we find that MILCA is more affected by foreground contamination. However, we also find that at large angular scales the diffuse Galactic dust contamination is significantly lower in the NILC-MILCA F/L cross-power spectrum than in the NILC F/L cross-power spectrum. This indicates that the residual dust contamination is not 100 % correlated between the reconstructed MILCA and NILC Compton parameter maps. In contrast, the clustered CIB and point source contamination levels are similar for the two cross-power spectra at high multipoles, indicating that the residual contamination is essentially 100% correlated between the MILCA and NILC maps.

### 5.2.1. Low-multipole contribution

The diffuse Galactic foreground contribution can be significantly reduced by choosing a more aggressive Galactic mask. Assuming that at large angular scales the Compton parameter maps are mainly affected by diffuse Galactic dust emission, we have tested several Galactic masks by imposing flux cuts on the *Planck* 857 GHz channel intensity map. In particular we investigated masking out 30%, 40%, 50%, 60%, and 70% of the sky. The edges of these masks have been apodized to limit ringing effects on the reconstruction of the angular power spectrum. Figure 5 presents the angular cross-power spectrum of the reconstructed NILC F/L Compton parameter maps for some of these Galactic masks: 30% (cyan); 40% (black); 50% (red); 60% (green); 70% (blue); and the PSMASK. We find that when masking 40% or more of the sky the tSZ angular power spectrum does not change significantly. That is why, conservatively, we select the 50% mask (GALMASK50 hereafter), which will be used in the remainder of our analysis.

We checked if the foreground contribution in the reconstructed *Planck* Compton parameter maps also depends on the reconstruction method. From the analysis of the FFP6 simulations we have found that the contribution from foregrounds in the NILC and MILCA Compton parameter maps is not the same, and it is not fully correlated. Similar results are found for the
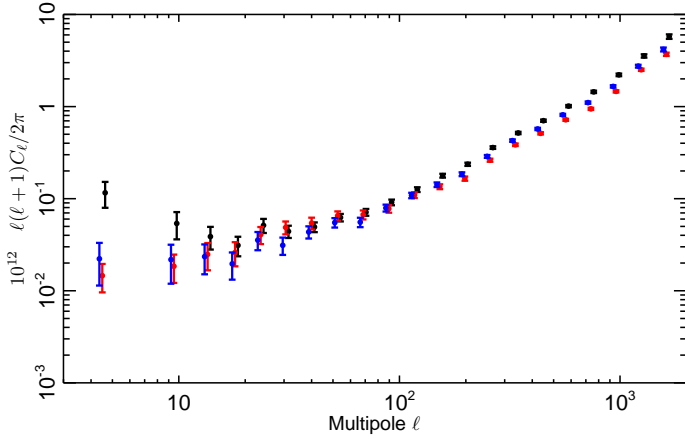
Fig. 6. Angular cross-power spectra between the reconstructed *Planck* MILCA F/L (black), NILC F/L (red), and NILC-MILCA F/L (blue) maps.
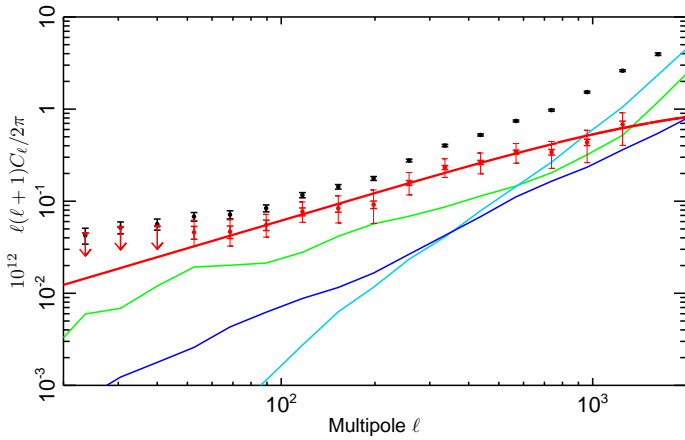
Fig. 7. NILC F/L cross-power spectrum before (black points) and after (red points) foreground correction, compared to the power spectra of the physically motivated foreground models. Specifically we show: clustered CIB (green line); infrared sources (cyan line); and radio sources (blue line). The statistical (thick line) and total (statistical plus foreground, thin line), uncertainties are also shown. Additionally we show the best-fit tSZ power spectrum model presented in Sect. 7.1 as a solid red line.

Planck data. Figure 6 shows the cross-power spectra between the MILCA F/L maps (black)[3], the NILC F/L maps (red) and the NILC- MILCA F/L maps (blue), as a function of ℓ. We observe that the MILCA F/L cross-power spectrum shows a larger amplitude than the NILC F/L cross-power spectrum. This is most probably due to a larger foreground contamination in the MILCA Compton parameter map.

In addition, we find that the NILC-MILCA F/L[4] cross-power spectrum shows the lowest amplitude at low multipoles ($\ell < 100$). This is due to a reduction of the dust contamination in the cross-correlation of the NILC and MILCA Compton parameter maps with respect to the dust contamination in the original maps. We also find that the NILC-MILCA F/L lies between the MILCA F/L and NILC F-L cross-power spectra at high multipoles. This can be explained by the differences in the clustered

---

[3] The excess of power at low ℓ observed in the MILCA F/L maps angular cross-power spectrum is due to the deconvolution from the extra low-multipole filtering in the MILCA maps, discussed in Sect. 4.1

[4] And equivalently MILCA-NILC F/L that is not shown in the Figure.

CIB contamination in the MILCA and NILC Compton parameter maps. An accurate model of the clustered CIB power spectrum is available. However, this is not the case for the dust contamination power spectrum, and thus we restrict the power spectrum analysis presented in Sect. 7.1 to $\ell > 60$.

Hereafter, we will consider the NILC F/L cross-power spectrum as a baseline for cosmological analysis, with the NILC-MILCA F/L cross-power spectrum being used to cross-check the results.

5.2.2. High-multipole contribution

The high-ℓ contamination from clustered CIB and point sources affects the measurement of the tSZ spectrum and its cosmological interpretation. Realistic models fitted to the *Planck* data are thus needed. We take advantage of the capability of *Planck* to measure and constrain these foreground emissions and use the outputs of Planck Collaboration XVIII (2011) and Planck Collaboration XXX (2013) for the clustered CIB modelling. For the six *Planck* HFI frequencies considered in this paper, the clustered CIB model consists of six auto-power spectra and 24 cross-power spectra. For frequencies above 217 GHz, these spectra are fitted in Planck Collaboration XXX (2013) to the measured CIB, consistently with Planck Collaboration XVIII (2011). The model is extrapolated at 100 and 143 GHz following Béthermin et al. (2012) and Planck Collaboration XVIII (2011). The uncertainties in the clustered-CIB model are mainly due to the cross-correlation coefficients that relate the cross-power spectra to the auto-power spectra. Following Planck Collaboration XXX (2013) we consider 5% global uncertainties on those coefficients.

We use the Béthermin et al. (2012) model to compute the star-forming dusty galaxy contribution. Finally, we use the Tucci et al. (2011) model, fitted to the *Planck* ERCSC (Planck Collaboration Int. VII 2013), for extragalactic radio sources. Notice that these models are also used for the study of the clustered CIB with *Planck* (Planck Collaboration XXX 2013).

We now estimate the residual power spectrum in the *y*-map after component separation. We apply the MILCA or NILC weights to Gaussian-realization maps drawn using the cross- and auto-spectra of each component at the six *Planck* HFI frequencies. The residual power spectrum in the *y*-map can also be estimated in the spherical harmonic domain, as detailed in Appendix A. We have tested the consistency between the two approaches and we give here results for a map-based estimate using a total of 50 all-sky simulations for each of the foreground components. Specific simulations, varying the foreground models, were also performed to propagate the 5% global uncertainties of the model-coefficients (which include the overall uncertainties in the CIB modelling) into the estimated residual power spectrum. We find a 50% uncertainty in the amplitude of each residual spectrum (clustered CIB, star-forming dusty galaxies, and radio sources) in the *y*-map.

Figure 7 shows the NILC F/L cross-power spectrum before (black points) and after (red points) foreground correction, using the refined foreground models presented above. We also show the clustered CIB (green), infrared source (cyan), and radio source (blue) power spectrum contributions.
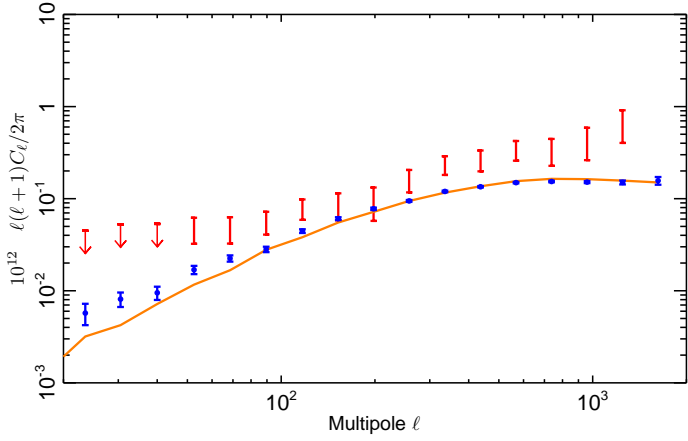
Fig. 8. Comparison of the tSZ angular power spectrum estimated from the cross-power-spectrum of the `NILC` F/L maps (black) with the expected angular power spectrum of the confirmed clusters in the *Planck* Cluster Sample (orange line). In red we plot the `NILC` F/L cross-power spectrum after masking these clusters. The green points correspond to the difference of these two cross-power spectra. The cross-power spectrum between the `NILC` Compton parameter map and the simulated detected cluster map is shown in blue.

5.3. Contribution of resolved clusters to the tSZ power spectrum

We simulate the expected Compton parameter map for the detected and confirmed clusters of galaxies in the *Planck* catalogue (Planck Collaboration XXIX 2013) from their measured integrated Compton parameter, Y_{5R500}. The orange solid line in Fig. 8 shows the power spectrum of this simulated map. Figure 8 also shows the cross-power spectrum of the `NILC` F/L maps (in black). In red we plot the cross-power spectrum of the `NILC` F/L maps after masking the confirmed clusters from the PSZ catalogue. The green curve corresponds to the difference of the two cross-power spectra, with and without masking the clusters. It is in good agreement with the modelled power spectrum of the confirmed clusters of galaxies. We also compute the cross-power spectrum of the simulated cluster map and the *Planck* reconstructed Compton parameter `NILC` map. This is shown in blue in the figure. Here again, the signal is consistent with the expected power spectrum of the confirmed *Planck* clusters of galaxies.

These results show that a significant fraction of the signal in the reconstructed *Planck* Compton parameter maps is due to the tSZ effect of detected and confirmed clusters of galaxies, verifying the SZ nature of the signal. In addition, by comparing the tSZ power spectrum from the resolved clusters with the marginalized tSZ power spectrum presented in Sect. 7, we deduce that the measured tSZ spectrum includes an additional tSZ contribution from unresolved clusters and diffuse hot gas.

6. Analysis of high-order statistics

The power spectrum analysis presented above only provides information on the 2-point statistics of the Compton parameter distribution over the sky. An extended characterization of the field can be performed by studying the higher-order moments in the 1D PDF of the map, or by measuring 3-point statistics, i.e., the bispectrum.
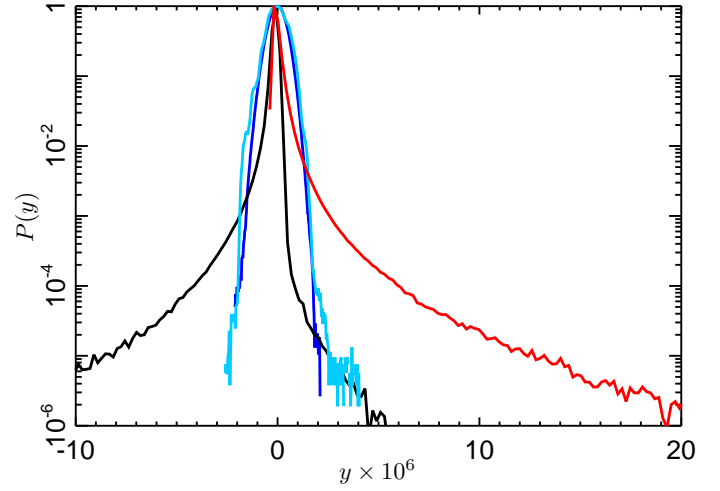
Fig. 9. 1D PDF for the `FFP6` simulation maps considering the `MILCA` linear combination weights obtained for the real data. The tSZ effect (red), diffuse Galactic emission (cyan), clustered CIB (blue), and radio source (black) contributions to the 1D PDF are shown.
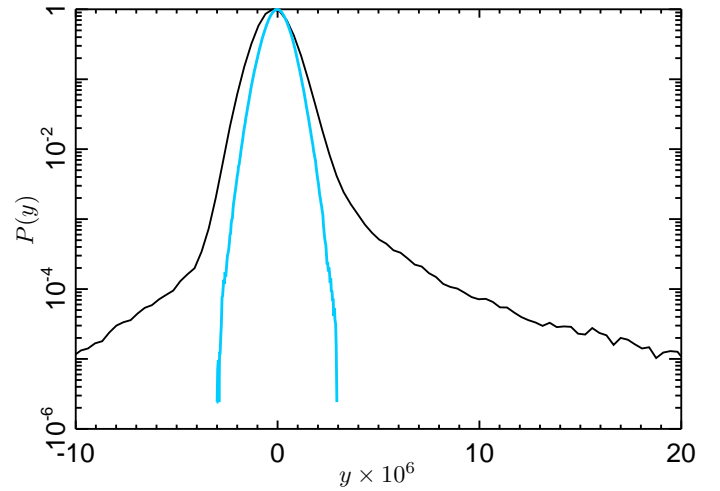
Fig. 10. 1D PDF of the *Planck* *y*-map (black) and of the null map (cyan) for the `MILCA` method.

6.1. 1D PDF analysis

We performed an analysis of the 1D PDF of the `NILC` and `MILCA` reconstructed Compton parameter maps. For the tSZ effect we expect an asymmetric distribution with a significantly positive tail (Rubiño-Martín & Sunyaev 2003). We thus focus on the asymmetry of the distribution and its unnormalized skewness. First, we filter the maps in order to enhance the tSZ signal with respect to foreground contamination and noise. To avoid residual point source ringing effects near the edges of the combined PSMASK and GALMASK50 masks we apodize them. We follow the approach of Wilson et al. (2012) and use a filter in harmonic space, constructed from the ratio between the angular power spectrum of the expected tSZ signal in the `FFP6` simulations and the power spectrum of the null *y* maps. We smooth this ratio using a 21-point square kernel and normalize it to one by dividing by its maximum value. Notice that this filter only selects the multipole range for which the tSZ signal is large with respect to the noise, and thus, it does not modify the non-Gaussianity properties. Furthermore, we have found that the filter used here

behaves better than the more traditionally used Wiener filter, as it is less affected by point-source ringing. Following this procedure, the 1D PDF of the filtered Compton parameter map, $P(y)$, is computed from the histogram of the pixels.

Figure 9 shows the 1D PDF for the `FFP6` simulation maps combined using the weights of the `MILCA` linear combination of the real data. We present in red the 1D PDF of the tSZ effect, which is clearly asymmetric, with a positive tail as expected. Moreover, the asymptotic slope of this red curve at high values of y scales almost as $P(y) \propto y^{-2.5}$, implying that the underlying source counts should scale in the same way (i.e., $dn/dy \propto y^{-2.5}$). This is the predicted scaling behaviour for clusters (e.g., de Luca et al. 1995; Rubiño-Martín & Sunyaev 2003), and indeed, it is the scaling that we find in the actual number counts of clusters in the simulation used. Similarly, the 1D PDF for radio sources (black) is also asymmetric, but with a negative tail. By contrast, the clustered CIB (blue) and diffuse Galactic emission (cyan) distributions are symmetric to first approximation. From this analysis we see that, as expected, the filtering enhances the tSZ effect with respect to foregrounds and therefore helps in their discrimination.

For illustration, Fig. 10 shows the 1D PDF for the `MILCA` Compton parameter map in black. This is the convolution of the 1D PDF of the different components in the map: the tSZ effect; foregrounds; and noise. Indeed, it clearly shows three distinct contributions: a Gaussian central part that exceeds slightly the contribution from noise, as expected from the null map 1D PDF (cyan curve); a small negative tail, corresponding most likely to residual radio sources; and a positive tail corresponding mainly to the tSZ signal. A direct computation of the slope of the full $P(y)$ function in Fig. 10 shows that it converges to -2.5 for $y > 10^{-5}$, as predicted from the cluster counts.

A simple analysis of the measured 1D PDF can be performed by considering the asymmetry of the distribution:

$$A \equiv \int_{y_p}^{+\infty} P(y)dy - \int_{-\infty}^{y_p} P(y)dy, \qquad (13)$$

where y_p is the peak value of the normalized distribution $(\int P(y)dy = 1)$. In addition, the non-Gaussianity of the positive tail can be quantified by

$$\Delta = \int_{y_p}^{+\infty} [P(y) - G(y)] \, dy, \qquad (14)$$

with $G(y)$ the expected distribution if fluctuations were only due to noise. For the `NILC` Compton parameter map we find $A = 0.185$ and $\Delta = 0.065$. Equivalently, for the `MILCA` Compton parameter map we find $A = 0.26$ and $\Delta = 0.11$. These results are consistent with a positive tail in the 1D PDF, as expected for the tSZ effect. The differences between the `NILC` and `MILCA` results come mainly from the difference in filtering. Similar values are obtained for the FFP6 simulations, with $A = 0.12$ and $\Delta = 0.05$ for NILC and $A = 0.30$ and $\Delta = 0.13$ for MILCA.

Alternatively, we can also compute the skewness of the obtained distribution, $\int y^3 P(y)dy / \left(\int y^2 P(y)dy \right)^{3/2}$. Following Wilson et al. (2012) we have chosen here a hybrid approach, by computing the unnormalized skewness of the filtered Compton parameter maps outside the 50% sky mask. In particular we have computed the skewness of the *Planck* data Compton parameter maps $\langle y^3 \rangle$, and of the null maps $\langle y^3_{\text{NULL}} \rangle$. For the `FFP6` simulations, we computed these for the tSZ component $\langle y^3_{\text{FFP6,SZ}} \rangle$ and for the sum of all astrophysical components $\langle y^3_{\text{FFP6,ALL}} \rangle$. Table 2

Table 2. Unnormalized skewness, multiplied by 10^{18}.

| Method	$\langle y^3 \rangle$	$\langle y^3_{\text{NULL}} \rangle$	$\langle y^3_{\text{FFP6,SZ}} \rangle$	$\langle y^3_{\text{FFP6,ALL}} \rangle$
NILC ...	1.78	-0.0001	2.17	2.09
MILCA ..	1.50	0.0004	1.46	1.21

shows the results for the `NILC` and `MILCA` maps. The different filtering function derived for the `NILC` and `MILCA` y-maps prevents a direct one-to-one comparison of the skewness values. However, the comparison of each map with the FFP6 simulations of the tSZ component and of the sum of all components clearly shows that the contribution of foregrounds is minor in both maps, and suggests that the measured skewness is mainly dominated by the tSZ signal, as one would expect from Figs. 9 and 10. By comparing the measured and model skewness, we present constraints on σ_8 in Sect. 7.2.
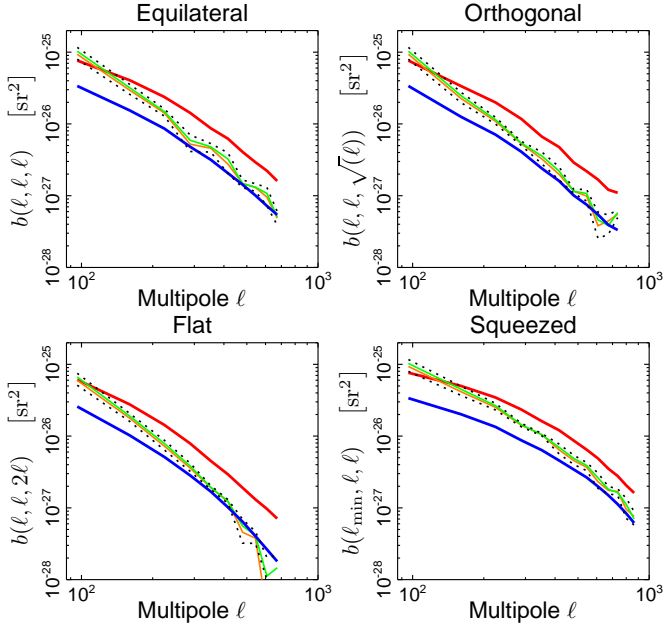
6.2. Bispectrum

Since the SZ signal is non-Gaussian, significant statistical information is contained in the bispectrum, complementary to the power spectrum (Rubiño-Martín & Sunyaev 2003; Bhattacharya et al. 2012). We therefore compute the bispectrum of the `NILC` and `MILCA` reconstructed Compton parameter maps. The results presented here use the binned bispectrum estimator described in Bucher et al. (2010) and Lacasa et al. (2012), which is also used for the *Planck* primordial non-Gaussianity analysis (Planck Collaboration XXIV 2013). We mask the maps with the combined PSMASK and GALMASK50, remove the best-fit monopole and dipole outside the mask, and degrade the resolution to $N_{\text{side}} = 1024$ to reduce computing time. We use a multipole bin size $\Delta\ell = 64$ and a maximum multipole $\ell_{\text{max}} = 2048$ for the analysis. To correct for the bias introduced by masking, we have produced non-Gaussian simulations with a tSZ-like bispectrum and we have convolved the simulated maps with a Gaussian beam of $10'$ FWHM. We compute the bispectrum of the simulated full-sky and masked maps and measure the average ratio between the two. This ratio is used to correct the measured bispectra and flag unreliable (ℓ_1, ℓ_2, ℓ_3) configurations, for which mask effects are too large to be corrected.

We checked that foreground residuals do not significantly affect the recovered tSZ bispectrum by using the `FFP6` simulations described previously. In the case of the `MILCA` reconstructed map (more affected by foregrounds), for example, Fig. 11 shows the tSZ bispectrum as well as the (absolute value of the) bispectra of the different foreground residuals. This is shown for some some special configurations, namely equilateral (ℓ, ℓ, ℓ), orthogonal isosceles $(\ell, \ell, \sqrt{2}\ell)$, flat isosceles $(\ell, \ell, 2\ell)$ and squeezed $(\ell_{\text{min}}, \ell, \ell)$. The foreground residuals yield negligible bispectra, at least one order of magnitude smaller than the tSZ bispectrum over the multipoles of interest.

In Fig. 12 we compare the tSZ bispectrum measured on *Planck* data, with the tSZ bispectrum of the `FFP6` simulation and with the bispectrum of the maps of detected clusters in the *Planck* catalogue presented above. Clusters from the *Planck* catalogue contribute an important fraction of the measured bispectrum, at least 30% on large angular scales and more on smaller angular scales; the bispectrum therefore also probes the unresolved tSZ signal, as was the case for the power spectrum. On large angular scales this may be the signature of the clustering of less massive dark matter halos inside the large-scale structures.
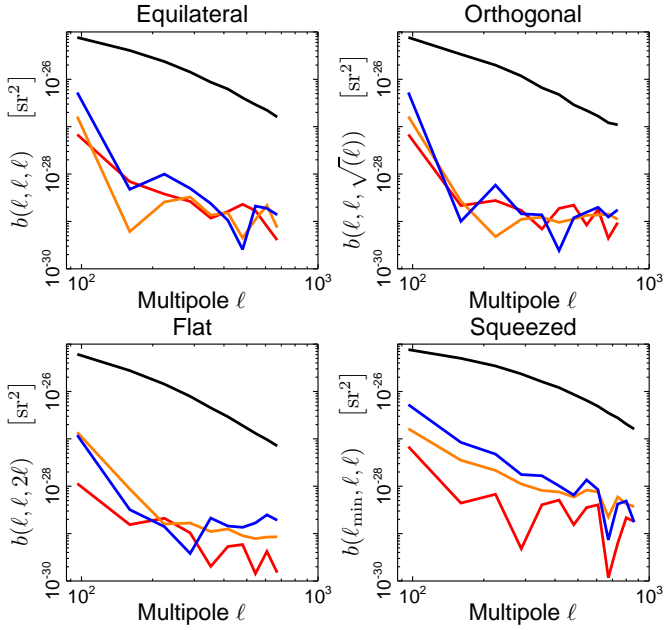
Fig. 11. Binned bispectra of the `FFP6` tSZ map, and foreground residuals for the `MILCA` component separation. The black line represents the tSZ bispectrum and the red line the clustered CIB. In addition, we plot the bispectrum for the Galactic diffuse free-free (orange), and the thermal dust (dark blue) emission.

Fig. 12. tSZ measured bispectra for the `MILCA` (green) and `NILC` (orange) Compton parameter maps, compared with the `FFP6` tSZ bispectrum (in red) and with the projected map of the catalogue of detected clusters (in blue). Uncertainties on the measured tSZ power bispectra are given by the dotted lines.

Alternatively large angular scales may be affected by foreground residuals.

Table 3. Marginalized bandpowers of the angular power spectrum of the *Planck* tSZ Compton parameter map (in dimensionless $(\Delta T/T)^2$ units), statistical and foreground errors, and best-fit tSZ power spectrum and number counts models (also dimensionless).

| ℓ_{min}	ℓ_{max}	ℓ_{eff}	$\ell(\ell+1)C_\ell/2\pi$ $[10^{12}y^2]$	σ_{stat} $[10^{12}y^2]$	σ_{fg} $[10^{12}y^2]$	Best-fit $[10^{12}y^2]$
21	27	23.5	< 0.045	...	...	0.014
27	35	30.5	< 0.052	...	...	0.019
35	46	40	< 0.053	...	...	0.025
46	60	52	0.046	0.007	$^{+0.014}_{-0.011}$	0.032
60	78	68	0.047	0.007	$^{+0.015}_{-0.012}$	0.042
78	102	89	0.056	0.007	$^{+0.015}_{-0.013}$	0.055
102	133	117	0.077	0.008	$^{+0.020}_{-0.016}$	0.072
133	173	152	0.084	0.008	$^{+0.029}_{-0.025}$	0.094
173	224	198	0.092	0.009	$^{+0.040}_{-0.033}$	0.121
224	292	257	0.158	0.009	$^{+0.046}_{-0.040}$	0.157
292	380	335	0.232	0.012	$^{+0.056}_{-0.050}$	0.203
380	494	436	0.264	0.013	$^{+0.069}_{-0.064}$	0.261
494	642	567	0.341	0.017	$^{+0.080}_{-0.081}$	0.332
642	835	738	0.340	0.024	$^{+0.102}_{-0.110}$	0.417
835	1085	959	0.436	0.035	$^{+0.149}_{-0.171}$	0.515
1085	1411	1247	0.681	0.059	$^{+0.222}_{-0.272}$	0.623

# 7. Cosmological Interpretation

7.1. Power spectrum analysis

As a measure of structure growth, the tSZ power spectrum can provide independent constraints on cosmological parameters and potentially improve their precision. As shown by Komatsu & Seljak (2002), the power spectrum of the tSZ effect is highly sensitive to the normalization of the matter power spectrum, commonly parameterized by the rms of the $z = 0$ mass distribution on $8\,h^{-1}$ Mpc scales, σ_8, and to the total amount of matter Ω_m. We expect the tSZ power spectrum to also be sensitive to other cosmological parameters, e.g., Ω_b, H_0, and n_s. For reasonable external priors on those parameters, however, the variations are expected to be negligible with respect to those introduced by changes in Ω_m and σ_8 and are not considered here. Finally, we also expect the tSZ power spectrum amplitude to be sensitive to the "mass bias", b. A full joint analysis cosmological parameters and mass bias is not possible with the current data and so we have chosen here to fix the mass bias to $b = 0.2$ following results in the companion Planck paper on cosmological constraints from Planck SZ cluster counts (Planck Collaboration XX 2013). Note that final cosmological constraints depend on this choice.

Cosmological constraints are obtained from a fit of the `NILC` F/L cross-power spectrum, for the 50% mask, assuming a three-component model: tSZ; clustered CIB; and radio and infrared point sources. For $\ell > 60$, we can reasonably neglect the Galactic dust contamination. For $\ell > 1411$ the total signal in the tSZ map is dominated by noise. We thus restrict our analysis to the multipole range $60 < \ell < 1411$. The measured power spectrum, C_ℓ^m, is modelled as:

$$C_\ell^m = C_\ell^{tSZ}(\Omega_m, \sigma_8) + A_{CIB}\, C_\ell^{CIB} + A_{PS}\, (C_\ell^{IR} + C_\ell^{Rad}). \tag{15}$$
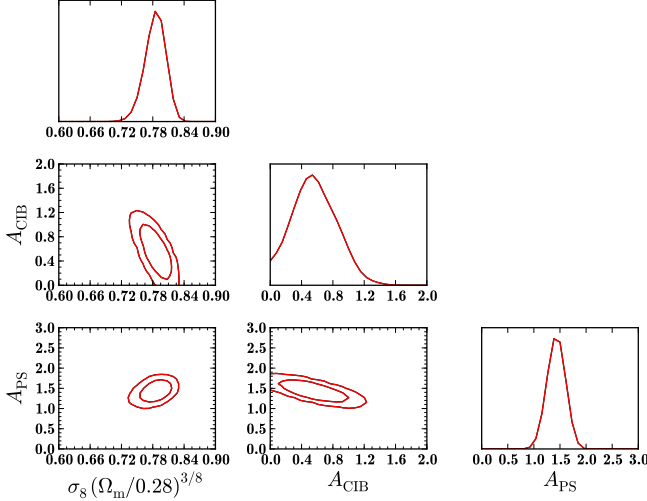
Fig. 13. 2D and 1D likelihood distributions for the combination of cosmological parameters $\sigma_8(\Omega_m/0.28)^{0.40}$, and for the foreground parameters A_{CIB} and A_{PS}. We show the 68.3% and 95.4% C.L. contours (in orange).
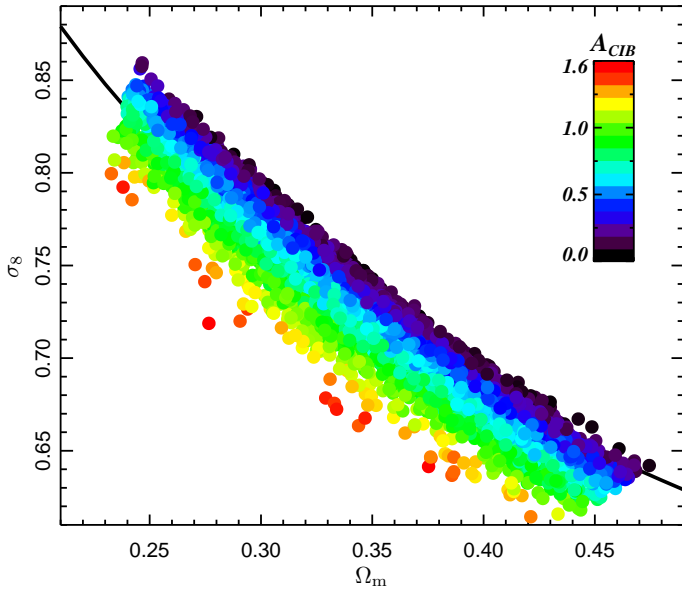
Fig. 14. Likelihood samples derived from the MCMC chains. The points represent pairs of values of Ω_m and σ_8. Only values within the 95.4% C.L. contours are shown. The clustered CIB amplitude is colour-coded according to the value of A_{CIB}, from low (blue) to high (red). The black solid line shows the theoretical degeneracy between the two cosmological parameters.

Here $C_\ell^{tSZ}(\Omega_m, \sigma_8)$ is the tSZ power spectrum, C_ℓ^{CIB} is the clustered CIB power spectrum, and C_ℓ^{IR} and C_ℓ^{Rad} are the infrared and radio source power spectra, respectively.

Following Eq. (8), the tSZ spectrum is computed using the 2-halo model, the Tinker et al. (2008) mass function, and the Arnaud et al. (2010) universal pressure profile. In particular, we use the numerical implementation presented in Taburet et al. (2009, 2010, 2011), and integrating in redshift from 0 to 3 and in mass from $10^{13}\,M_\odot$ to $5 \times 10^{15}\,M_\odot$. Our model allows us to

compute the tSZ power spectrum at the largest angular scales. It is consistent with the tSZ spectrum presented in Efstathiou & Migliaccio (2012), which was used as a template in the CMB cosmological analysis in Planck Collaboration XV (2013) and Planck Collaboration XVI (2013).

Foreground contamination is modelled following Sect. 5.2.2. As discussed there, the main uncertainties in the residual power spectrum translate into up to 50% uncertainty in the clustered CIB and point source amplitudes. We thus allow for a variation of the normalization amplitudes for the clustered CIB, A_{CIB}, and for the point sources, A_{PS}, with Gaussian priors centred on 1 with standard deviation 0.5.

We have not considered explicitly the expected correlation between the tSZ effect and the CIB. However, using the formalism in Addison et al. (2012), we have performed simulations of the expected effect and find that to a reasonable level of approximation the shape of the tSZ and clustered CIB cross-power spectrum is very similar to that of the clustered CIB power spectrum. Therefore, in our simplified modelling, the clustered CIB normalization factor, A_{CIB}, also accounts for this component.

We assume a Gaussian approximation for the likelihood function. Best-fit values and uncertainties are obtained using an adapted version of the `Cosmo-MC` algorithm (Lewis & Bridle 2002). Only σ_8 and Ω_m are allowed to vary here. All other cosmological parameters are fixed to their best-fit values as obtained in Table 2 of Planck Collaboration XVI (2013). The normalization amplitudes, A_{CIB} and A_{PS}, considered as nuisance parameters, are allowed to vary between 0 and 3. For the range of multipoles considered here, the tSZ angular power spectrum varies like $C_\ell \propto \sigma_8^{8.1}\Omega_m^{3.2}$. The results are thus presented in terms of this parameter combination.

Figure 13 presents the 2D and 1D likelihood distributions for the cosmological parameter combination $\sigma_8\Omega_m^{3.2/8.1}$, or equivalently $\sigma_8\Omega_m^{0.40}$ and for the foreground nuisance parameters. The best-fit values and error bars for each parameter are given by $\sigma_8(\Omega_m/0.28)^{0.40} = 0.784 \pm 0.016$, $\sigma_8 = 0.74 \pm 0.06$, $\Omega_m = 0.33 \pm 0.06$, $A_{CIB} = 0.55 \pm 0.26$, and $A_{PS} = 0.14 \pm 0.13$. It is worth noting that these values are obtained in a specific framework, all other cosmological parameters being fixed and a fiducial fixed model used for the signals. Relaxing this framework would likely weaken the constraints presented in this paper.

Figure 14 shows the degeneracy between the two cosmological parameters from the Monte Carlo Markov chains (MCMC), as well as the theoretical degeneracy (solid black line). It also shows the dependency on A_{CIB} (colour coded from low values in blue to high values in red). While the combination $\sigma_8(\Omega_m/0.28)^{0.40}$ is well determined, marginalized constraints on σ_8 and Ω_m are weaker. To check the robustness of our results, we performed the same cosmological analysis using the `NILC-MILCA` F/L cross-power spectrum presented in Fig. 6. Although the foreground level is different, we find compatible results at the $1\,\sigma$ level. Furthermore, our constraints are in good agreement with those derived from the *Planck* cluster number count analysis (Planck Collaboration XX 2013), which shows a similar σ_8–Ω_m degeneracy line. Conversely, our findings exhibit some tension with the constraints derived from the *Planck* primary CMB analysis (Planck Collaboration XVI 2013), which finds larger values of σ_8 and Ω_m. However, as discussed in Planck Collaboration XX (2013), the constraints from the SZ signal depend significantly on the assumed value of the mass bias.

The red points in Fig. 15 correspond to the marginalized *Planck* tSZ power spectrum (from the `NILC` F/L cross-power spectrum), compared to the best-fit theoretical model presented above (solid red line). Foreground uncertainties are derived from
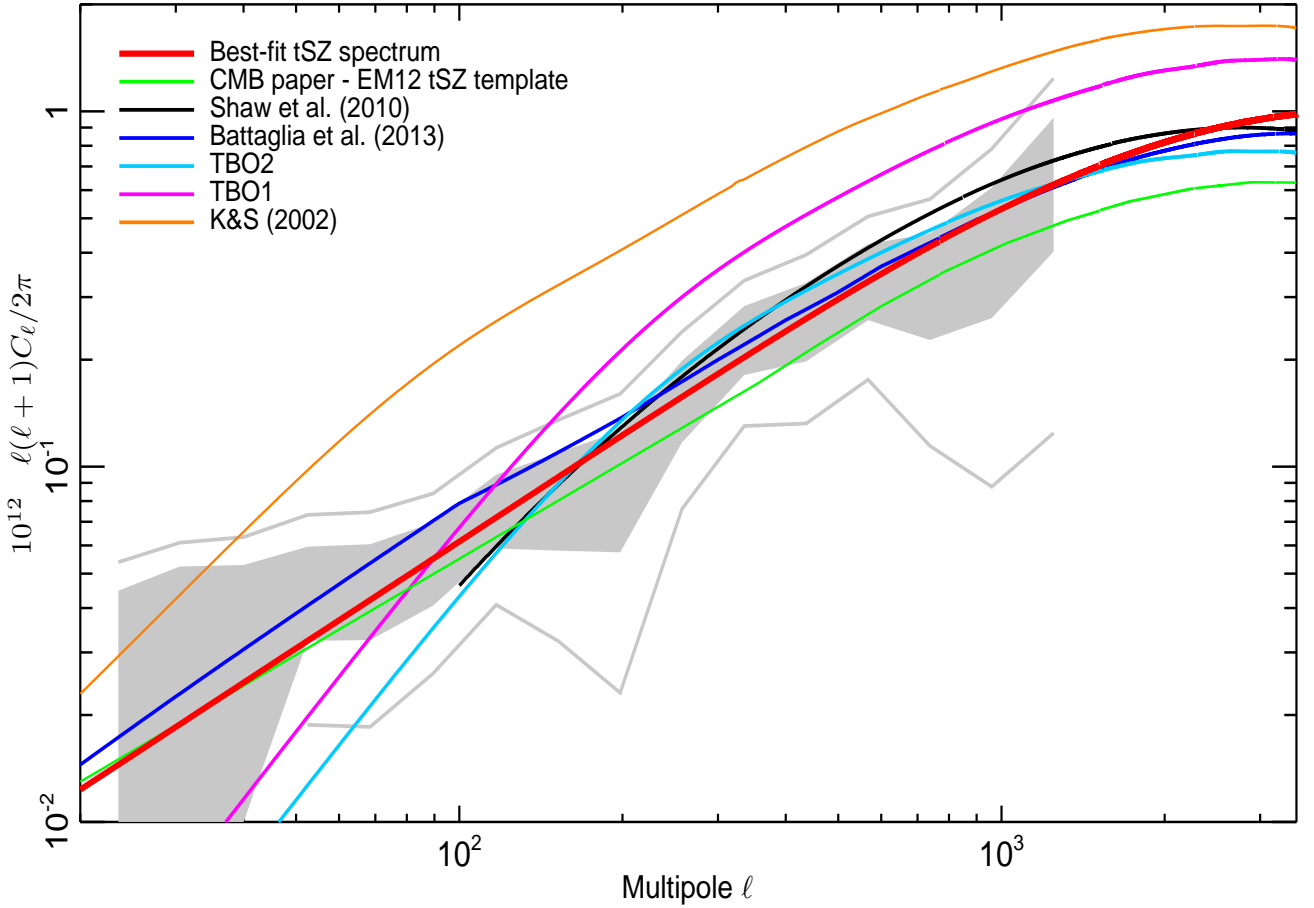
Fig. 15. Marginalized bandpowers of the *Planck* tSZ power spectrum with total (statistical plus foreground) uncertainties (red points). The red solid line represents the best-fit tSZ power spectrum model. We also show as a blue solid line the best-ft tSZ power spectrum obtained from the analysis of cluster number counts (Planck Collaboration XX 2013). The tSZ power spectrum template used in the CMB cosmological analysis (Planck Collaboration XV 2013; Planck Collaboration XVI 2013) is presented as a green solid line. For comparison, we also show the SPT (Reichardt et al. 2012, orange diamond) and ACT (Sievers et al. 2013, cyan diamond) constraints on the tSZ power spectrum at $\ell = 3000$.

the likelihood curves of the nuisance parameters and added in quadrature to the statistical uncertainties, providing the total errors plotted here. Table 3 presents the *Planck* marginalized tSZ power spectrum, together with statistical and foreground uncertainties, and the best-fit tSZ power spectrum model. In the range $\ell = 60$–1411, the *Planck* tSZ power spectrum can be approximated by a power law of the form

$$\ell(\ell + 1)C_\ell/2\pi = (1.0 \pm 0.2) \times 10^{-15}\ell^{(0.91\pm0.03)}. \qquad (16)$$

The measured tSZ power spectrum is in remarkable agreement with the tSZ power spectrum (blue solid line) computed using the cluster count best-fit parameters (Planck Collaboration XX 2013). We also show in Fig. 15 (green line) the tSZ template used in the *Planck* CMB analysis Planck Collaboration XVI (2013). This template is renormalized by a simple scaling factor using the best-fit $\sigma_8(\Omega_{\rm m}/0.28)^{0.40}$ The difference in shapes of the two spectra is due to the different assumptions used for the scaling relation between SZ signal and mass (see, Efstathiou & Migliaccio 2012). We also show the SPT (Reichardt et al. 2012, orange diamond) and ACT (Sievers et al. 2013, cyan diamond) constraints on the tSZ power spectrum at $\ell = 3000$, which are consistent with our best-fit model within $\pm2\sigma$ and illustrate that the tSZ spectrum starts to turn over at higher ℓ.

In Fig. 16, we compare the *Planck* tSZ measurements of the power spectrum to a set of predicted spectra. We consider the predictions derived from hydrodynamical simulations (Battaglia et al. 2010; Battaglia et al. 2012, brown), from *N*-body simulations plus semi-analytical models (Trac et al. 2011, purple and cyan) and from analytical calculations (Shaw et al. 2010, black; Komatsu & Seljak 2002, orange). These models were computed originally for the set of cosmological parameters in Hinshaw et al. (2012) with $\sigma_8 = 0.8$ and have been rescaled in amplitude to our best-fit value for $\sigma_8^{8.1}\Omega_{\rm m}^{3.2}$. We note that there is some dispersion in the predicted amplitudes and shapes of the tSZ power spectrum. These differences reflect the range of methodologies and assumptions used both in the physical properties of clusters and in the technical details of the computation. The latter includes differences in the redshift ranges and also in the mass intervals probed by the limited sizes of the simulation boxes of the hydrodynamical simulations. Analytical predictions are also sensitive to the model ingredients, such as the mass function, mass bias and scaling relations adopted.

We see from Fig. 16 that most of the models presented above (the tSZ template for CMB analyses, plus the Battaglia et al. 2012, Shaw et al. 2010 and TBO2 models) provide reasonable fits to the data, while the others (TBO1 and Komatsu & Seljak
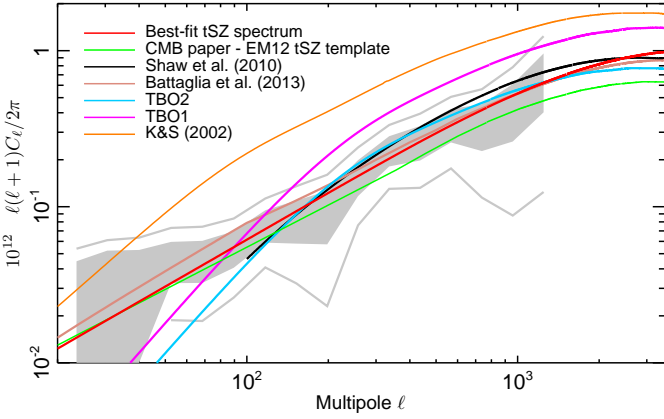
Fig. 16. Comparison of the *Planck* tSZ power spectrum and best-fit model with existing models in the literature. The *Planck* tSZ power spectrum and the ±1 and 2 σ error bars are shown in grey. We also show the *Planck* tSZ power spectrum best-fit models derived in this paper (red) and from the analysis of cluster number counts (Planck Collaboration XX 2013, blue). The tSZ power spectrum template used in the CMB cosmological analysis (Planck Collaboration XV 2013; Planck Collaboration XVI 2013, green) is also shown. We additionally show the tSZ power spectrum models from hydrodynamic simulations (Battaglia et al. 2012, brown), from *N*-body simulations plus semi-analytical dust gas models (Trac et al. 2011, cyan; TBO1 and purple; TBO2), and from analytical calculations (Shaw et al. 2010, black; Komatsu & Seljak 2002, orange).

2002) are clearly not consistent. The TBO1 model was a highly simplified approach superseded by TBO2 (Trac et al. 2011). The Komatsu & Seljak (2002) prediction shows a significantly different shape compared with all the other models; this is not well understood and we will not consider it further. We have performed a simplified likelihood analysis to evaluate the uncertainties in cosmological parameters induced by the uncertainties in the modelling of the cluster physics. We replace our own model of the tSZ power spectrum by the models discussed above (excluding the TBO1 and Komatsu & Seljak 2002 ones) and re-compute $\sigma_8(\Omega_m/0.28)^{0.40}$, A_{CIB}, and A_{PS} from a simple linear fit to the NILC F/L cross-power spectrum. We obtain values for $\sigma_8(\Omega_m/0.28)^{0.40}$ between 0.768 and 0.798, which lie within the 1 σ uncertainties (0.016) presented above.

The *Planck* data allow us for the first time to probe the large and intermediate angular scales ($\ell = 46$ to $\ell = 1085$) for the tSZ spectrum; furthermore, and, as shown in Planck Collaboration XXIX (2013), *Planck* is particularly sensitive to the SZ signal from massive clusters not probed by other experiments. The *Planck* tSZ measurement will hence permit us to better understand the integrated tSZ contribution of the whole population of clusters, including resolved and nearby clusters, the correlated SZ signal, and possible diffuse hot gas.

7.2. High-order statistics

The estimates of tSZ non-Gaussianity, e.g., the unnormalized skewness and bispectrum, are very sensitive to σ_8. Using the models presented in Sect. 3 we can show that the unnormalized skewness of the tSZ fluctuation, $\langle T^3(\mathbf{n}) \rangle$ scales approximately as σ_8^{11}, whereas the amplitude of the bispectrum scales as σ_8^α with $\alpha = 11$–12, as shown by Bhattacharya et al. (2012). We do

not consider in the following the dependency of the bispectrum and the unnormalized skewness on other cosmological parameters, since all such dependencies are expected to be significantly lower than for σ_8 (Bhattacharya et al. 2012).

We derive constraints on σ_8 by comparing the measured unnormalized skewness and bispectrum amplitudes with those obtained from simulations of the tSZ effect. This approach is strongly limited by systematic uncertainties and the details of the theoretical modelling (see Hill & Sherwin 2013).

From the measured unnormalized skewness of the filtered MILCA and NILC Compton parameter maps discussed in Sect. 6.1 and by comparing them to the value measured in the FFP6 simulations we can derive constraints on σ_8. Uncertainties due to foreground contamination are computed using the FFP6 simulations and are accounted for in the final error bars. The tSZ component of the FFP6 simulations was obtained from a hybrid simulation including a hydrodynamic component for $z < 0.3$ plus extra individual clusters at $z > 0.3$, and with $\sigma_8 = 0.789$. Using these simulations we obtain $\sigma_8 = 0.775$ for NILC and $\sigma_8 = 0.783$ for MILCA. Combining the two results and considering model and foreground uncertainties we obtain $\sigma_8 = 0.779 \pm 0.015(68\%$ C.L.). Notice that the uncertainties are mainly dominated by foreground contamination. Model uncertainties here only account for the expected dependence of the unnormalized skewness upon σ_8, as shown in Sect. 3. We have neglected, as was also the case in Wilson et al. (2012), the dependence on other cosmological parameters. We have also not considered any uncertainties coming from the combination of the hydrodynamical and individual cluster simulations. Because of these constraints, our error bars might be underestimated.

The comparison of the measured bispectrum obtained from the *Planck* Compton parameter maps with the FFP6 simulation tSZ bispectrum shows an offset of about a factor of two on small angular scales, $300 < \ell < 700$, which we attribute to the differences in cosmological parameters. Using the scaling of the bispectrum with σ_8, its uncertainty, as well as the uncertainty on the bispectra ratio, we obtain $\sigma_8 = 0.74 \pm 0.04(68\%$ C.L.). As was the case for the unnormalized skewness, we neglected here the dependence on other cosmological parameters and the uncertainties in the FFP6 simulations. Thus the error bar might again be somewhat underestimated. However, we expect those additional uncertainties to be smaller than the error bars we quote.

8. Conclusion

Because of its wide frequency coverage from 30 to 857 GHz, the *Planck* satellite mission is particularly well suited for the measurement of the thermal Sunyaev-Zeldovich effect. Working with the *Planck* frequency channel maps from 100 to 857 GHz, we have reconstructed the tSZ signal over the full sky using tailored component separation methods. In this paper, we have analysed the first all-sky tSZ map quantified in terms of the Compton parameter and with an angular resolution of 10′.

We have characterized the reconstructed *Planck* all-sky Compton parameter map in terms of blind detection of tSZ sources, and the angular power spectrum and higher order statistics via the study of its 1D PDF and bispectrum. In all cases we have identified, characterized and carefully modelled the contamination by foreground emission. This is mainly due to diffuse Galactic thermal dust emission at large angular scales ($\ell \lesssim 60$), and clustered CIB and Poisson-distributed radio and infrared sources at smaller angular scales (dominating at $\ell \gtrsim 500$). Diffuse Galactic thermal dust emission is tackled via a conservative masking of the brightest 50% of the sky in the *Planck*

857 GHz channel map. The CIB and point-source contamination are modelled in a way which is consistent with the findings of Planck Collaboration XVIII (2011) and Planck Collaboration XXX (2013).

We have produced the first measurement of the SZ power spectrum on large angular scales, ranging over $0.17° \lesssim \theta \lesssim 3.0°$. In this range, the tSZ power spectrum is almost insensitive to the physics of cluster cores. The detected tSZ signal likely arises from the contribution of warm and hot diffuse gas distributed within groups and clusters, sampling the whole halo mass function, as well as within the larger-scale filamentary structures.

We have modelled the tSZ power spectrum via a halo-model analytical approach, in order investigate its dependence on σ_8 and Ω_m and to test it against the measured *Planck* tSZ power spectrum. Moreover, we performed an analysis of the 1D PDF and bispectrum of the *Planck* *y*-map to infer independent constraints. We find, in the present framework, that the best-fit normalization parameter σ_8 from the three independent analysis ranges between (0.74 ± 0.06) and (0.78 ± 0.02) at 68% C.L. for the high-order statistics and power spectrum analyses, respectively.

These values are lower than those derived from analysis of primary CMB anisotropies (Planck Collaboration XVI 2013). More refined analysis and modelling will be needed to understand this difference, since the tension may have several possible origins. Some of the difference may be due to specific choices in the tSZ modelling, e.g., the mass bias (see Planck Collaboration XX 2013, for a detailed discussion on its effect of its effect on cluster counts). Other differences could arise from the foreground modelling, in particular at high frequencies, above 217 GHz.

The observed consistency between constraints derived from the cluster number counts in Planck Collaboration XX (2013) and from the present work provides a coherent view of the gas content in halos and in larger-scale structures. As such, this *Planck* tSZ measurement constitutes the first step towards building a comprehensive understanding of the integrated tSZ effect due to cosmic structure on all scales and at all density contrasts.

References

Addison, G. E., Dunkley, J., & Spergel, D. N. 2012, MNRAS, 427, 1741

Arnaud, M., Pratt, G. W., Piffaretti, R., et al. 2010, A&A, 517, A92

Battaglia, N., Bond, J. R., Pfrommer, C., & Sievers, J. L. 2012, ApJ, 758, 75

Battaglia, N., Bond, J. R., Pfrommer, C., Sievers, J. L., & Sijacki, D. 2010, ApJ, 725, 91

Benson, B. A., de Haan, T., Dudley, J. P., et al. 2013, ApJ, 763, 147

Bertin, E. & Arnouts, S. 1996, A&AS, 117, 393

Béthermin, M., Daddi, E., Magdis, G., et al. 2012, ApJ, 757, L23

Bhattacharya, S., Nagai, D., Shaw, L., Crawford, T., & Holder, G. P. 2012, ApJ, 760, 5

Bucher, M., Tent, B. V., & Carvalho, C. S. 2010, MNRAS, 407, 2193

Carlstrom, J. E., Holder, G. P., & Reese, E. D. 2002, ARA&A, 40, 643

Carvalho, P., Rocha, G., Hobson, M. P., & Lasenby, A. 2012, MNRAS, 427, 1384

Crawford, T. M., Schaffer, K. K., Bhattacharya, S., et al. 2013, ApJ submitted, arXiv:1303.3535

Das, S., Louis, T., Nolta, M. R., et al. 2013, eprint arXiv, 1301, 1037

de Luca, A., Desert, F. X., & Puget, J. L. 1995, A&A, 300, 335

Delabrouille, J., Betoule, M., Melin, J.-B., et al. 2013, A&A, 553, A96

Delabrouille, J., Cardoso, J.-F., Jeune, M. L., et al. 2009, A&A, 493, 835

Diego, J. M. & Majumdar, S. 2004, MNRAS, 352, 993

Dunkley, J., Calabrese, E., Sievers, J., et al. 2013, eprint arXiv, 1301, 776

Efstathiou, G. & Migliaccio, M. 2012, MNRAS, 423, 2492

González-Nuevo, J., Argüeso, F., López-Caniego, M., et al. 2006, MNRAS, 369, 1603

Górski, K. M., Hivon, E., Banday, A. J., et al. 2005, ApJ, 622, 759

Hasselfield, M., Hilton, M., Marriage, T. A., et al. 2013, eprint arXiv, 1301, 816, 32 pages, 21 figures

Herranz, D., Sanz, J. L., Hobson, M. P., et al. 2002, MNRAS, 336, 1057

Hill, J. C. & Sherwin, B. D. 2013, PRD, 87, 23527

Hinshaw, G., Larson, D., Komatsu, E., et al. 2012, eprint arXiv, 1212, 5226

Hivon, E., Górski, K. M., Netterfield, C. B., et al. 2002, ApJ, 567, 2

Hurier, G., Hildebrandt, S. R., & Macias-Perez, J. F. 2013, A&A in press, arXiv:1007.1149

Komatsu, E. & Kitayama, T. 1999, ApJ, 526, L1

Komatsu, E. & Seljak, U. 2002, MNRAS, 336, 1256

Komatsu, E. & Seljak, U. 2002, MNRAS, 336, 1256

Lacasa, F., Aghanim, N., Kunz, M., & Frommert, M. 2012, MNRAS, 421, 1982

Lewis, A. & Bridle, S. 2002, Phys. Rev. D, 66, 103511

López-Caniego, M., Herranz, D., González-Nuevo, J., et al. 2006, MNRAS, 370, 2047

Mak, D. S. Y. & Pierpaoli, E. 2012, PRD, 86, 123520

Melin, J., Bartlett, J. G., & Delabrouille, J. 2006a, A&A, 459, 341

Melin, J.-B., Aghanim, N., Bartelmann, M., et al. 2012, Astronomy & Astrophysics, 548, 51

Melin, J.-B., Bartlett, J. G., & Delabrouille, J. 2006b, A&A, 459, 341

Mo, H. J. & White, S. D. M. 1996, MNRAS, 282, 347

Planck Collaboration ES. 2013, The Explanatory Supplement to the Planck 2013 results (ESA)

Planck Collaboration I. 2013, Submitted to A&A

Planck Collaboration II. 2013, Submitted to A&A

Planck Collaboration III. 2013, Submitted to A&A

Planck Collaboration Int. VII. 2013, A&A, 550, A133

Planck Collaboration IV. 2013, Submitted to A&A

Planck Collaboration IX. 2013, Submitted to A&A

Planck Collaboration V. 2013, Submitted to A&A

Planck Collaboration VI. 2013, Submitted to A&A

Planck Collaboration VII. 2013, Submitted to A&A

Planck Collaboration VIII. 2011, A&A, 536, A8

Planck Collaboration VIII. 2013, Submitted to A&A

Planck Collaboration X. 2011, A&A, 536, A10

Planck Collaboration XI. 2011, A&A, 536, A11

Planck Collaboration XII. 2011, A&A, 536, A12

Planck Collaboration XII. 2013, Submitted to A&A

Planck Collaboration XV. 2013, Submitted to A&A

Planck Collaboration XVI. 2013, Submitted to A&A

Planck Collaboration XVIII. 2011, A&A, 536, A18

Planck Collaboration XX. 2013, Submitted to A&A

Planck Collaboration XXIV. 2013, Submitted to A&A

Planck Collaboration XXIX. 2013, Submitted to A&A

Planck Collaboration XXVIII. 2013, Submitted to A&A

Planck Collaboration XXX. 2013, Submitted to A&A

Reichardt, C. L., Shaw, L., Zahn, O., et al. 2012, ApJ, 755, 70

Reichardt, C. L., Stalder, B., Bleem, L. E., et al. 2013, ApJ, 763, 127

Remazeilles, M., Delabrouille, J., & Cardoso, J.-F. 2011, MNRAS, 410, 2481

Rubiño-Martín, J. A. & Sunyaev, R. A. 2003, MNRAS, 344, 1155

Shaw, L. D., Nagai, D., Bhattacharya, S., & Lau, E. T. 2010, ApJ, 725, 1452

Sievers, J. L., Hlozek, R. A., Nolta, M. R., et al. 2013, eprint arXiv, 1301, 824

Sunyaev, R. A. & Zeldovich, Y. B. 1972, Comments on Astrophysics and Space Physics, 4, 173

Taburet, N., Aghanim, N., Douspis, M., & Langer, M. 2009, mnras, 392, 1153

Taburet, N., Douspis, M., & Aghanim, N. 2010, MNRAS, 404, 1197

Taburet, N., Hernández-Monteagudo, C., Aghanim, N., Douspis, M., & Sunyaev, R. A. 2011, MNRAS, 418, 2207

Tinker, J., Kravtsov, A. V., Klypin, A., et al. 2008, ApJ, 688, 709

Tinker, J., Kravtsov, A. V., Klypin, A., et al. 2008, ApJ, 688, 709

Trac, H., Bode, P., & Ostriker, J. P. 2011, ApJ, 727, 94

Tristram, M., Macías-Pérez, J. F., Renault, C., & Santos, D. 2005, MNRAS, 358, 833

Tucci, M., Toffolatti, L., de Zotti, G., & Martínez-González, E. 2011, A&A, 533, A57

Wilson, M. J., Sherwin, B. D., Hill, J. C., et al. 2012, PRD, 86, 122005

Appendix A: Foreground contamination in the final tSZ power spectrum

Since we are using modified Internal Linear Combination methods to estimate the final *Planck* Compton parameter map we can write it as

$$\hat{y}(\theta, \phi) = \sum_{\nu} \sum_{b} W_{\nu}^{b}(\theta, \phi)\left(F^{b}(\theta, \phi) * M_{\nu}(\theta, \phi)\right), \qquad (A.1)$$

where $M_{\nu}(\theta, \phi)$ is the *Planck* map for frequency channel ν, $F^{b}(\theta, \phi)$ is a circular filtering function for the multipole interval b, and $W_{\nu}^{b}(\theta, \phi)$ are the weights of the internal linear combination into that multipole range. Decomposing $\hat{y}(\theta, \phi)$ in spherical harmonics we obtain

$$\hat{y}_{\ell, m} = \sum_{\nu} \sum_{b} W_{\nu\,\ell, m; \ell', m'}^{b} F_{\ell'}^{b} * M_{\nu\ell', m'}. \qquad (A.2)$$

Then using spherical harmonic convolution properties (see for example Tristram et al. 2005) and assuming overlap in the multipole range selected by the filter functions, F_{ℓ}^{b}, then the power spectrum is given by

$$C_{\ell}^{y, y} = \sum_{b} \sum_{b'} \sum_{\nu} \sum_{\nu'} \sum_{\ell'} \mathcal{M}_{\ell, \ell'}^{W_{\nu}^{b}, W_{\nu'}^{b'}} F_{\ell'}^{b} F_{\ell'}^{b'} C_{\ell'}^{M_{\nu}, M_{\nu'}}, \qquad (A.3)$$

where $\mathcal{M}_{\ell, \ell'}^{W_{\nu}^{b}, W_{\nu'}^{b'}}$ represents the mode-coupling matrix associated with $W_{\nu}^{b} \times W_{\nu'}^{b'}$.

For each *Planck* channel the sky signal can be expressed as the sum of multiple components, including CMB, tSZ, diffuse Galactic emission, radio and IR point sources, and clustered CIB, such that the *Planck* Compton parameter is given by

$$\hat{y} = y + y^{\text{CMB}} + \sum_{c} y^{c}, \qquad (A.4)$$

where c sums over the different foreground contributions. By construction $y_{\text{CMB}} = 0$ and thus, assuming no correlation between foreground components, the estimated tSZ spectrum can be expressed as

$$C_{\ell}^{\hat{y}, \hat{y}} = C_{\ell}^{\text{tSZ}} + \sum_{c} C_{\ell}^{y^{c}, y^{c}}. \qquad (A.5)$$

Using Eq. (A.1) we write

$$y^{c}(\theta, \phi) = \sum_{\nu} \sum_{b} W_{\nu}^{b}(\theta, \phi)\left(F^{b}(\theta, \phi) * M_{\nu}^{c}(\theta, \phi)\right), \qquad (A.6)$$

and thus, using Eq. (A.3), we have

$$C_{\ell}^{y^{c}, y^{c}} = \sum_{b} \sum_{b'} \sum_{\nu} \sum_{\nu'} \sum_{\ell'} \mathcal{M}_{\ell, \ell'}^{W_{\nu}^{b}, W_{\nu'}^{b}} F_{\ell'}^{b} F_{\ell'}^{b} C_{\ell'}^{M_{\nu}^{c}, M_{\nu'}^{c}}. \qquad (A.7)$$

The latter expression can be simplified assuming a common spatial distribution of the foreground emission across frequencies and a well defined spectral energy density, f_{ν}^{c}, so that it reads

$$C_{\ell}^{y^{c}, y^{c}} = \sum_{b} \sum_{\nu} \sum_{\nu'} \sum_{\ell'} \mathcal{M}_{\ell, \ell'}^{W_{\nu}^{b}, W_{\nu'}^{b'}} F_{\ell'}^{b} F_{\ell'}^{b'} f_{\nu}^{c} f_{\nu'}^{c} C_{\ell'}^{M^{c}, M^{c}}. \qquad (A.8)$$

Let us now look at the cross-correlation between the estimated Compton parameter map and a particular sky component at one of the observation frequencies $M_{c}^{\nu'}(\theta, \phi) = \sum_{\ell m} T_{c; \ell m}^{\nu} Y_{\ell m}(\theta, \phi)$. We define the cross-power spectrum as

$$C_{\ell}^{\hat{y}, c}(\nu) = \frac{1}{2\ell + 1} \sum_{m=-\ell}^{\ell} \hat{y}_{\ell m} M_{c; \ell m}^{\nu*} \qquad (A.9)$$

and the statistical expectation of this quantity reads

$$\left\langle C_{\ell}^{\hat{y}, c}(\nu) \right\rangle = \frac{1}{2\ell + 1} \sum_{m=-\ell}^{\ell} \sum_{b, \nu'} \sum_{\ell'm'} W_{\ell\ell'; mm'}^{b\nu'} F_{\ell'}^{b} \left\langle M_{\ell'm'}^{\nu'} M_{c, \ell m}^{\nu*} \right\rangle \quad (A.10)$$

$$= \frac{1}{2\ell + 1} \sum_{m=-\ell}^{\ell} \sum_{b, \nu'} \sum_{\ell'm'} W_{\ell\ell'; mm'}^{b\nu'} F_{\ell'}^{b} C_{c; \ell}^{\nu\nu'} \delta_{\ell\ell'} \delta_{mm'} \quad (A.11)$$

$$= \frac{1}{2\ell + 1} \sum_{m=-\ell}^{\ell} \sum_{b, \nu'} W_{\ell\ell; mm}^{b\nu'} F_{\ell}^{b} C_{c; \ell}^{\nu\nu'}. \qquad (A.12)$$

Assuming that we have a measure of $C_{c; \ell}^{\nu\nu'}$ and a way to derive $W_{\ell\ell; mm}^{b\nu'} F_{\ell}^{b}$, we can compare the measured cross-correlation $\hat{y} \times c$ to its theoretical expectation and thus have a consistency check on each component's contribution to $\hat{y}$.

[1] APC, AstroParticule et Cosmologie, Université Paris Diderot, CNRS/IN2P3, CEA/lrfu, Observatoire de Paris, Sorbonne Paris Cité, 10, rue Alice Domon et Léonie Duquet, 75205 Paris Cedex 13, France

[2] Aalto University Metsähovi Radio Observatory, Metsähovintie 114, FIN-02540 Kylmälä, Finland

[3] African Institute for Mathematical Sciences, 6-8 Melrose Road, Muizenberg, Cape Town, South Africa

[4] Agenzia Spaziale Italiana Science Data Center, Via del Politecnico snc, 00133, Roma, Italy

[5] Agenzia Spaziale Italiana, Viale Liegi 26, Roma, Italy

[6] Astrophysics Group, Cavendish Laboratory, University of Cambridge, J J Thomson Avenue, Cambridge CB3 0HE, U.K.

[7] Astrophysics & Cosmology Research Unit, School of Mathematics, Statistics & Computer Science, University of KwaZulu-Natal, Westville Campus, Private Bag X54001, Durban 4000, South Africa

[8] Atacama Large Millimeter/submillimeter Array, ALMA Santiago Central Offices, Alonso de Cordova 3107, Vitacura, Casilla 763 0355, Santiago, Chile

[9] CITA, University of Toronto, 60 St. George St., Toronto, ON M5S 3H8, Canada

[10] CNRS, IRAP, 9 Av. colonel Roche, BP 44346, F-31028 Toulouse cedex 4, France

[11] California Institute of Technology, Pasadena, California, U.S.A.

[12] Centre for Theoretical Cosmology, DAMTP, University of Cambridge, Wilberforce Road, Cambridge CB3 0WA, U.K.

[13] Centro de Astrofísica, Universidade do Porto, Rua das Estrelas, 4150-762 Porto, Portugal

[14] Centro de Estudios de Física del Cosmos de Aragón (CEFCA), Plaza San Juan, 1, planta 2, E-44001, Teruel, Spain

[15] Computational Cosmology Center, Lawrence Berkeley National Laboratory, Berkeley, California, U.S.A.

[16] Consejo Superior de Investigaciones Científicas (CSIC), Madrid, Spain

[17] DSM/Irfu/SPP, CEA-Saclay, F-91191 Gif-sur-Yvette Cedex, France

[18] DTU Space, National Space Institute, Technical University of Denmark, Elektrovej 327, DK-2800 Kgs. Lyngby, Denmark

[19] Département de Physique Théorique, Université de Genève, 24, Quai E. Ansermet,1211 Genève 4, Switzerland

[20] Departamento de Física Fundamental, Facultad de Ciencias, Universidad de Salamanca, 37008 Salamanca, Spain

[21] Departamento de Física, Universidad de Oviedo, Avda. Calvo Sotelo s/n, Oviedo, Spain

[22] Department of Astronomy and Astrophysics, University of Toronto, 50 Saint George Street, Toronto, Ontario, Canada

[23] Department of Astrophysics/IMAPP, Radboud University Nijmegen, P.O. Box 9010, 6500 GL Nijmegen, The Netherlands

[24] Department of Electrical Engineering and Computer Sciences, University of California, Berkeley, California, U.S.A.

[25] Department of Physics & Astronomy, University of British Columbia, 6224 Agricultural Road, Vancouver, British Columbia, Canada

[26] Department of Physics and Astronomy, Dana and David Dornsife College of Letter, Arts and Sciences, University of Southern California, Los Angeles, CA 90089, U.S.A.

[27] Department of Physics and Astronomy, University College London, London WC1E 6BT, U.K.

[28] Department of Physics, Florida State University, Keen Physics Building, 77 Chieftan Way, Tallahassee, Florida, U.S.A.

[29] Department of Physics, Gustaf Hällströmin katu 2a, University of Helsinki, Helsinki, Finland

[30] Department of Physics, Princeton University, Princeton, New Jersey, U.S.A.

[31] Department of Physics, University of California, One Shields Avenue, Davis, California, U.S.A.

[32] Department of Physics, University of California, Santa Barbara, California, U.S.A.

[33] Department of Physics, University of Illinois at Urbana-Champaign, 1110 West Green Street, Urbana, Illinois, U.S.A.

[34] Dipartimento di Fisica e Astronomia G. Galilei, Università degli Studi di Padova, via Marzolo 8, 35131 Padova, Italy

[35] Dipartimento di Fisica e Scienze della Terra, Università di Ferrara, Via Saragat 1, 44122 Ferrara, Italy

[36] Dipartimento di Fisica, Università La Sapienza, P. le A. Moro 2, Roma, Italy

[37] Dipartimento di Fisica, Università degli Studi di Milano, Via Celoria, 16, Milano, Italy

[38] Dipartimento di Fisica, Università degli Studi di Trieste, via A. Valerio 2, Trieste, Italy

[39] Dipartimento di Fisica, Università di Roma Tor Vergata, Via della Ricerca Scientifica, 1, Roma, Italy

[40] Discovery Center, Niels Bohr Institute, Blegdamsvej 17, Copenhagen, Denmark

[41] Dpto. Astrofísica, Universidad de La Laguna (ULL), E-38206 La Laguna, Tenerife, Spain

[42] European Southern Observatory, ESO Vitacura, Alonso de Cordova 3107, Vitacura, Casilla 19001, Santiago, Chile

[43] European Space Agency, ESAC, Planck Science Office, Camino bajo del Castillo, s/n, Urbanización Villafranca del Castillo, Villanueva de la Cañada, Madrid, Spain

[44] European Space Agency, ESTEC, Keplerlaan 1, 2201 AZ Noordwijk, The Netherlands

[45] Finnish Centre for Astronomy with ESO (FINCA), University of Turku, Väisäläntie 20, FIN-21500, Piikkiö, Finland

[46] Haverford College Astronomy Department, 370 Lancaster Avenue, Haverford, Pennsylvania, U.S.A.

[47] Helsinki Institute of Physics, Gustaf Hällströmin katu 2, University of Helsinki, Helsinki, Finland

[48] INAF - Osservatorio Astrofisico di Catania, Via S. Sofia 78, Catania, Italy

[49] INAF - Osservatorio Astronomico di Padova, Vicolo dell'Osservatorio 5, Padova, Italy

[50] INAF - Osservatorio Astronomico di Roma, via di Frascati 33, Monte Porzio Catone, Italy

[51] INAF - Osservatorio Astronomico di Trieste, Via G.B. Tiepolo 11, Trieste, Italy

[52] INAF Istituto di Radioastronomia, Via P. Gobetti 101, 40129 Bologna, Italy

[53] INAF/IASF Bologna, Via Gobetti 101, Bologna, Italy

[54] INAF/IASF Milano, Via E. Bassini 15, Milano, Italy

[55] INFN, Sezione di Bologna, Via Irnerio 46, I-40126, Bologna, Italy

[56] INFN, Sezione di Roma 1, Università di Roma Sapienza, Piazzale Aldo Moro 2, 00185, Roma, Italy

[57] IPAG: Institut de Planétologie et d'Astrophysique de Grenoble, Université Joseph Fourier, Grenoble 1 / CNRS-INSU, UMR 5274, Grenoble, F-38041, France

[58] IUCAA, Post Bag 4, Ganeshkhind, Pune University Campus, Pune 411 007, India

[59] Imperial College London, Astrophysics group, Blackett Laboratory, Prince Consort Road, London, SW7 2AZ, U.K.

[60] Infrared Processing and Analysis Center, California Institute of Technology, Pasadena, CA 91125, U.S.A.

[61] Institut Néel, CNRS, Université Joseph Fourier Grenoble I, 25 rue des Martyrs, Grenoble, France

[62] Institut Universitaire de France, 103, bd Saint-Michel, 75005, Paris, France

[63] Institut d'Astrophysique Spatiale, CNRS (UMR8617) Université Paris-Sud 11, Bâtiment 121, Orsay, France

[64] Institut d'Astrophysique de Paris, CNRS (UMR7095), 98 bis Boulevard Arago, F-75014, Paris, France

[65] Institute for Space Sciences, Bucharest-Magurale, Romania

[66] Institute of Astronomy and Astrophysics, Academia Sinica, Taipei, Taiwan

[67] Institute of Astronomy, University of Cambridge, Madingley Road, Cambridge CB3 0HA, U.K.

[68] Institute of Theoretical Astrophysics, University of Oslo, Blindern, Oslo, Norway

[69] Instituto de Astrofísica de Canarias, C/Vía Láctea s/n, La Laguna, Tenerife, Spain

[70] Instituto de Física de Cantabria (CSIC-Universidad de Cantabria), Avda. de los Castros s/n, Santander, Spain

[71] Jet Propulsion Laboratory, California Institute of Technology, 4800 Oak Grove Drive, Pasadena, California, U.S.A.

[72] Jodrell Bank Centre for Astrophysics, Alan Turing Building, School of Physics and Astronomy, The University of Manchester, Oxford Road, Manchester, M13 9PL, U.K.

[73] Kavli Institute for Cosmology Cambridge, Madingley Road, Cambridge, CB3 0HA, U.K.

[74] LAL, Université Paris-Sud, CNRS/IN2P3, Orsay, France

[75] LERMA, CNRS, Observatoire de Paris, 61 Avenue de l'Observatoire, Paris, France

[76] Laboratoire AIM, IRFU/Service d'Astrophysique - CEA/DSM - CNRS - Université Paris Diderot, Bât. 709, CEA-Saclay, F-91191 Gif-sur-Yvette Cedex, France

[77] Laboratoire Traitement et Communication de l'Information, CNRS (UMR 5141) and Télécom ParisTech, 46 rue Barrault F-75634 Paris Cedex 13, France

[78] Laboratoire de Physique Subatomique et de Cosmologie, Université Joseph Fourier Grenoble I, CNRS/IN2P3, Institut National Polytechnique de Grenoble, 53 rue des Martyrs, 38026 Grenoble cedex, France

[79] Laboratoire de Physique Théorique, Université Paris-Sud 11 & CNRS, Bâtiment 210, 91405 Orsay, France

[80] Lawrence Berkeley National Laboratory, Berkeley, California, U.S.A.

[81] Max-Planck-Institut für Astrophysik, Karl-Schwarzschild-Str. 1, 85741 Garching, Germany

[82] McGill Physics, Ernest Rutherford Physics Building, McGill University, 3600 rue University, Montréal, QC, H3A 2T8, Canada

[83] MilliLab, VTT Technical Research Centre of Finland, Tietotie 3, Espoo, Finland

[84] Niels Bohr Institute, Blegdamsvej 17, Copenhagen, Denmark

[85] Observational Cosmology, Mail Stop 367-17, California Institute of Technology, Pasadena, CA, 91125, U.S.A.

[86] Optical Science Laboratory, University College London, Gower Street, London, U.K.

[87] SB-ITP-LPPC, EPFL, CH-1015, Lausanne, Switzerland

[88] SISSA, Astrophysics Sector, via Bonomea 265, 34136, Trieste, Italy

[89] School of Physics and Astronomy, Cardiff University, Queens Buildings, The Parade, Cardiff, CF24 3AA, U.K.

[90] School of Physics and Astronomy, University of Nottingham, Nottingham NG7 2RD, U.K.

[91] Space Research Institute (IKI), Russian Academy of Sciences, Profsoyuznaya Str, 84/32, Moscow, 117997, Russia

[92] Space Sciences Laboratory, University of California, Berkeley, California, U.S.A.

[93] Special Astrophysical Observatory, Russian Academy of Sciences, Nizhnij Arkhyz, Zelenchukskiy region, Karachai-Cherkessian Republic, 369167, Russia

[94] Stanford University, Dept of Physics, Varian Physics Bldg, 382 Via Pueblo Mall, Stanford, California, U.S.A.

[95] Sub-Department of Astrophysics, University of Oxford, Keble Road, Oxford OX1 3RH, U.K.

[96] Theory Division, PH-TH, CERN, CH-1211, Geneva 23, Switzerland

[97] UPMC Univ Paris 06, UMR7095, 98 bis Boulevard Arago, F-75014, Paris, France

[98] Université de Toulouse, UPS-OMP, IRAP, F-31028 Toulouse cedex 4, France

[99] University Observatory, Ludwig Maximilian University of Munich, Scheinerstrasse 1, 81679 Munich, Germany

[100] University of Granada, Departamento de Física Teórica y del Cosmos, Facultad de Ciencias, Granada, Spain

[101] Warsaw University Observatory, Aleje Ujazdowskie 4, 00-478 Warszawa, Poland